Global and Planetary Change 177 (2019) 81–100

Contents lists available at ScienceDirect

Global and Planetary Change

journal homepage: www.elsevier.com/locate/gloplacha

Research article

What caused Earth's largest mass extinction event? New evidence from the Permian-Triassic boundary in northeastern Utah

Benjamin J. Burger[a,*], Margarita Vargas Estrada[b], Mae Sexauer Gustin[b]

[a] Department of Geology, Utah State University Uintah Basin Campus, 320 North Aggie Blvd., Vernal, UT 84078, USA
[b] Department of Natural Resources and Environmental Science (MS 186), University of Nevada-Reno, Reno, NV 89557, USA

ABSTRACT

The discovery of a Permian-Triassic boundary section in northeastern Utah provided an opportunity to study the chemistry and geology associated with this event that led to one of the greatest mass extinctions on the planet. From 83% to 97% of the species living on the planet went extinct during this relatively short interval of geological time that defines the major geological boundary between the Paleozoic and Mesozoic Eras. The cause and resulting sequence of events that led to this extinction have puzzled geologists for years. The new stratigraphic section in Utah provided a framework for reconstruction of the chemistry that was in the ocean during the mass extinction. Geochemical analysis of the section demonstrates, moving across the boundary from the Paleozoic to the Mesozoic, a significant drop in carbonate and total organic carbon, and a delayed occurrence of pyrite. Carbon isotope ratios ($\delta^{13}C$) show a negative excursion in carbonate with ratios dropping from 2.59‰ to −3.63‰. Elevated mercury is present at the boundary with a 4-fold increase from background levels. The boundary layer also has elevated zinc, lead, strontium, and nickel, but not at high enough levels to indicate a volcanic ash source. There is no evidence in concentrations of siderophile and chalcophile elements for an extraterrestrial impact. The stratigraphic section in Utah supports the theory of a massive release of carbon dioxide, resulting in the acidification of the oceans. High levels of mercury, as well as elevated levels of zinc and lead, implicate a coal source triggered by the contemporary Siberian Traps sill complex. The delay of enriched sulfur and barium content in the stratigraphic record indicates an anoxic ocean and upwelling of methane hydrates from depth. Further study of this stratigraphic section will aid our understanding of the global impact these catastrophic events had on life.

1. Introduction

In 2002, Alvarez and O'Connor (2002) challenged geologists working in the American Southwest to locate the Permian-Triassic boundary. The boundary, however, proved elusive, as many of the studied outcrops in western Utah and eastern Nevada demonstrated unconformities resulting in a hiatus across the boundary interval (Paull and Paull, 1982). In the Great Basin of western Utah, the boundary is often represented by a conglomerate atop erosional Permian rock layers. Sperling and Ingle (2006) were the first to document a continuous Permian-Triassic section based solely on carbon isotopes in northern Nevada in the deeper marine facies of the Quinn River Formation. Study of Late Permian and Early Triassic rocks in southeastern Idaho has also suggested a possible boundary section (Wignall and Hallam, 1992), although often these sections have been interpreted as drowning unconformities due to rapid changes in sea level (Paull and Paull, 1994) or faulted by subsequent tectonic activity (Paull and Paull, 1982). Rocks in southeastern Idaho and extending to southcentral Utah preserve remarkable Early Triassic (Smithian) marine faunas (Schubert and Bottjer, 1995; Fraiser and Bottjer, 2007; Brayard et al., 2017), which record the biological recovery following the mass extinction event. However, well preserved shallow marine Permian-Triassic boundary sections along the western coastline of Pangea have been elusive until now. This study provides detailed geochemistry across a newly discovered Permian-Triassic boundary stratigraphic section in northeastern Utah. The newly discovered section on the western coastline of Pangea offers a new regional look at the changing chemistry of the Panthalassic Ocean. This is the first section of the boundary from the shallow-marine western coastline of Pangea at an equatorial paleolatitude.

The newly discovered boundary section is located along the northern flank of the Uinta Mountains in northeastern Utah along Sheep Creek Valley, which preserves a thick sequence of Late Permian and Early Triassic rock layers (Fig. 1). The local area has previously received little attention, despite the well exposed outcrops of the earliest Triassic (Gresbachian) Dinwoody Formation, and latest Permian Park City Formation. The new Utah stratigraphic section across the Permian-Triassic boundary is compared geochemically with other stratigraphic sections, particularly those from the Global Boundary Stratotype Section and Point (GSSP) in Meishan, South China (Yin et al., 2001).

Geochemical signals documented from other sections across the Permian-Triassic Boundary provide a method for the identification of the boundary within the localized section in Utah. These observations include: 1) a significant drop in Total Organic Carbon (TOC) due to loss

* Corresponding author.
E-mail address: benjamin.burger@usu.edu (B.J. Burger).

https://doi.org/10.1016/j.gloplacha.2019.03.013
Received 26 February 2018; Received in revised form 6 December 2018; Accepted 20 March 2019
Available online 23 March 2019
0921-8181/ © 2019 Published by Elsevier B.V.

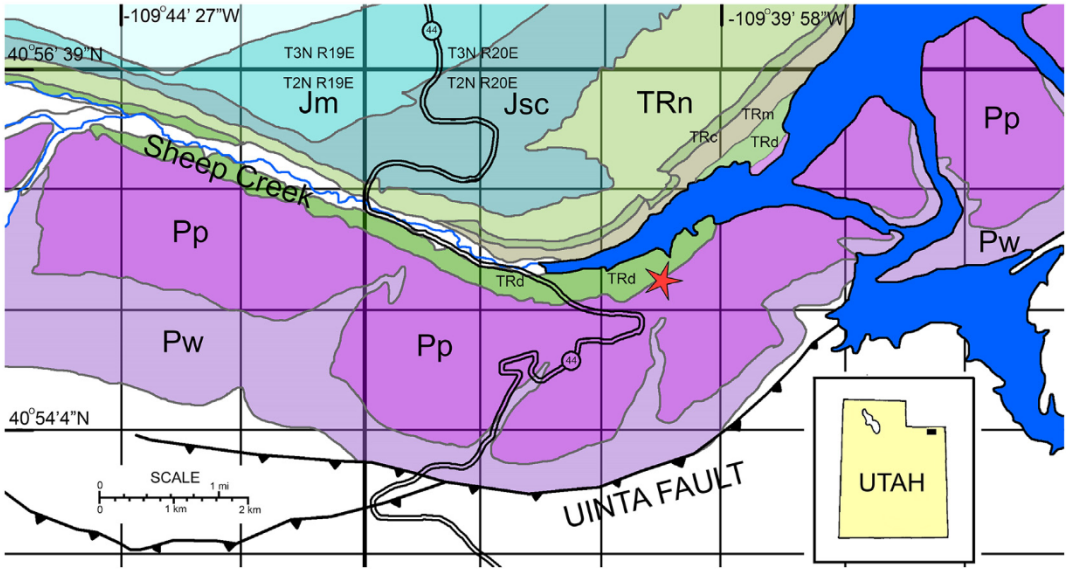

Fig. 1. Simplified geological map of Sheep Creek Valley showing location of the Permian-Triassic stratigraphic section. (Pw), Permian Weber Formation. (Pp), Permian Park City Formation. (TRd), Triassic Dinwoody Formation. (TRm), Triassic Moenkopi Formation. (TRc), Triassic Chinle Formation. (TRn), Triassic Nugget Formation. (Jsc), Jurassic Stump/Curtis Formation. (Jm), Jurassic Morrison Formation.

of bio-productivity (Korte et al., 2004; Krull et al., 2004; Berner, 2006; Sanei et al., 2012), but not observed in high-latitude sections in New Zealand and Canada (Krull et al., 2000; Schoepfer et al., 2012), and 2) a negative carbon isotope excursion, with carbonate ratios ($\delta^{13}C$) dropping from ranges between 4.0 and 3.0‰ VPDB to between −1.0 and −3.0‰ VPDB during the Permian-Triassic extinction event, indicating a ^{12}C enriched carbon source, such as hydrocarbon, entering the carbon cycle and being subsequently deposited across the boundary (Jin et al., 2000; Riccardi et al., 2007; Sun et al., 2012).

Other observations of the Permian-Triassic boundary include 3) the presence of pyrite in marine sediments indicating an anoxic event that was remarkably shallow and sudden during the interval (Wignall and Hallam, 1992; Wignall and Twitchett, 2002; Wignall et al., 2005; Shen et al., 2007; Kakuwa, 2008; Bond and Wignall, 2010; Brennecka et al., 2011; Schoepfer et al., 2012; Schoepfer et al., 2013; Liao et al., 2017; Huang et al., 2019), and 4) a dramatic decrease in carbonate deposition indicating increasing acidity in the world's ocean, and shallowing of the carbonate compensation depth (CCD; Kakuwa, 1996; Kershaw et al., 1999; Payne et al., 2007). More recently discovered indicators include 5) a 3-fold increase in mercury (Hg) restricted to the boundary layer (Sanei et al., 2012; Grasby et al., 2016; Grasby et al., 2017; Wang et al., 2018); and 6) a 3 to 10-fold increase in nickel (Ni) and zinc (Zn) within the boundary layer (Liu et al., 2017; Rampino et al., 2017), which is interpreted as a result of volcanic ash fallout from the Siberian Traps large igneous province eruptions (Le Vaillant et al., 2017).

1.1. Geological setting

Bounded by the Permian Park City Limestone and Triassic Nugget Sandstone, the Sheep Creek Valley is a short valley formed by a tributary of the Green River, which runs along the bedding plane of the softer shale and mudstone rock layers, in the northeastern corner of Utah near the town of Manila (Fig. 1). The valley borders the Flaming Gorge Reservoir on the north side of the Uinta Mountain Range, with rock beds dipping 19 to 30° toward the north and strikes bearing east-west, parallel to the axis of the mountain range. The Flaming Gorge Reservoir forms a freshwater flooded embayment into the valley downstream toward the east, while the upslope western end of the Sheep Creek Valley narrows into the Sheep Creek Canyon Geological Area managed by the U.S. Forest Service (Sprinkel et al., 2000). Paleozoic formations in the valley include the Weber Sandstone and Park City Limestone, while the Mesozoic formations are represented by the Triassic Dinwoody, Moenkopi, Chinle and Nugget formations, with Jurassic and Cretaceous units exposed toward the north (Fig. 1).

Biozonation of the latest Permian and earliest Triassic units in Utah based on conodont biostratigraphy indicate that the Permian-Triassic boundary is located at the base of the Dinwoody Formation. The earliest Triassic conodont biozone (Biozone 1 of Sweet and Bergström, 1986) composed of the species *Hideodus typicalis, Isarcicella isarcica, and Hideodus parvus* is recognized in the lower Dinwoody Formation (lowest 10 m of the formation) by the reported occurrence of both *Hideodus typicalis* and *Isarcicella isarcica* (Paull, 1988). The upper Park City Formation contains the conodont species *Merrillina divergens* (Biozone 8 of Wardlaw and Collinson, 1986), indicating a latest Permian age. *Merrillina divergens* ranges from the earliest Wuchiapingian to late Changhsingian ages of the latest Permian (Henderson, 2018).

Biozonation of the latest Permian and earliest Triassic units in Utah based on cephalopod biostratigraphy also indicates that the Permian-Triassic boundary is located near the base of the Dinwoody Formation. The Park City and Phosphoria Formations contain characteristic Late Permian ammonites (*Stacheoceras*, *Gastrioceras*, *Goniatites*, and *Waagenoceras*) and nautiloid *Coelogasteroceras* (Miller and Cline, 1934; Newell and Kummel, 1942). While the overlaying Dinwoody Formation contains characteristic lower Griesbachian ammonites (*Otoceras*, *Discophiceras*, *Metophiceras*) of the basal Triassic (Newell and Kummel, 1942). Other later occurring Early Triassic ammonites (*Meekoceras*, *Columbites*, *Tirolites*, *Genodiscus*, *Juvenites*, *Arctoceras*, *Euflemingites*, *Xenodiscoides*, *Dieneroceras*, *Metacoceras*) are well known from the overlaying Smithian-Spathian Thaynes Limestone (Smith, 1969), which is correlative to the Moenkopi Formation in the local section (Kummel, 1954). Dated zircon crystals within the overlaying Moenkopi Formation in northern Utah suggest an early Smithian age for the unit (Heckert et al., 2015).

Brachiopod extinction across the Permian-Triassic boundary is apparent in the occurrence of fossils in the Park City and Dinwoody Formations. The Park City exhibits a diverse fauna of brachiopods, including the following genera (*Neospirifer, Composita, Hystricula, Chonetes, Derbyia, Spiriferina, Hustedia, Orbiculoides, Sphenosteges, Bathymyonia, Horridonia, Echinauris, Wellerella, Phricodonthyris, Hustedia, Muirwoodia, Rugatia, Kochiproductus, Crurithyris, Cancrinella, Lingula* and *Leiorhynchus)*, of these only *Lingula* is well documented in the overlaying Dinwoody Formation (Newell and Kummel, 1942;

Yochelson, 1968; Smith, 1969; Wardlaw and Collinson, 1979; Hofmann et al., 2013). Several other brachiopods have been reported in the upper Dinwoody Formation, including *Mentzelia,* and *Spiriferina* (Newell and Kummel, 1942). However, *Lingula* is by far the most dominate brachiopod in the Dinwoody Formation (Hofmann et al., 2013). Newell and Kummel (1942) recognized a middle *Lingula*-zone of the Dinwoody Formation, just above the local section. *Lingula* is the only recognizable brachiopod reported within the lower Dinwoody Formation (Hofmann et al., 2013).

Bivalves show a profound turnover near the lithologic contact between the Park City and Dinwoody Formations. The Park City Formation exhibits the following bivalve genera (*Allorisma*, *Astartella*, *Aviculopecten*, *Myalina*, *Myalinella*, *Nuculopsis*, *Polidevcia*, *Schizodus*, *Streblochondria*, and *Wilkingia*; Yochelson, 1968). Of these only *Myalinella* extends into the Dinwoody Formation, with the Early Triassic species *Myalinella postcarbonica* found in the upper Dinwoody Formation (Hofmann et al., 2013). Bivalves faired better during the end-Permian extinction, and there are a number of species reported from the upper Dinwoody Formation indicating an Early Triassic age, including *Promyalina spathi*, *Promyalina putiatinensis*, *Myalinella postcarbonica, Eumorphotis multiformis, Eumorphotis amplicostata, Leptochondria occidanea, Permophorus bregeri, Unionites fassaensis, Neoschizodus laevigatus, Austrotindaria canalensis* (Newell and Kummel, 1942; Hofmann et al., 2013). However, the most common bivalve in the upper Dinwoody Formation is *Claraia* that is recognized in the upper *Claraia*-zone of the Dinwoody Formation (Newell and Kummel, 1942), where three species are known (*C. stachei, C. mulleri, C. aurita*; Hofmann et al., 2013). Fossil bivalves in the lower Dinwoody Formation are extremely rare and difficult to find.

Gastropods are represented in the Park City Formation by five genera (*Naticopsis*, *Cyclites*, *Orthonema*, and *Babylonites*) indicative of the Late Permian (Yochelson, 1968). There are no reported occurrences of gastropods in the lower Dinwoody Formation, nor in the middle *Lingula*-zone. Two reported gastropods are known in the upper Dinwoody Formation, (*Dicellonema abrekensis* and *Coelostylina* sp.) indicative of the Early Triassic (Hofmann et al., 2013).

Unidentified crinoid and bryozoan fossils are documented in the Park City Formation (Yochelson, 1968), but are so far absent from the Dinwoody Formation. Above the Dinwoody Formation, in the overlaying upper Thaynes Limestone is a dominate fauna of the echinoderm *Pentacrinus*, indicative of the Triassic period (Smith, 1969).

1.2. Stratigraphic section studied

Located at 40°55′15.016″ latitude, 109°40′22.026″ longitude, the new Permian-Triassic section encompasses a thickness of 9 m that brackets the lithologic boundary between the Franson Member of the Park City Formation and lower Dinwoody Formation (Fig. 2). High resolution geochemical sampling every 5 cm was carried out from 50 cm below up to 200 cm above the lithologic contact. Additional samples were collected with a spacing of 50 cm from above and below this high resolution sampled zone, within the 9-m section (Fig. 2). The stratigraphic section can be divided into five distinct zones based on color and lithology. The lowest zone (samples P-450 to P − 5) represents a yellowish gray (Munsell 5Y 8/1) limestone (pelmicrite/pellet wackestone), representing the upper facies (Franson Member) of the Permian Park City Formation. At the top of this zone, within 5 cm just below the lithologic contact (sample P-0), the limestone contains small crystals of hematite, which shifts the color to a grayish orange pink (Munsell 5YR 7/2). This upper contact layer has an undulating surface, but lacks any evidence of karstification or dissolution due to contact with meteoric water. This 5 cm layer was found to contain abundant Fe and Mn oxides through ICP-MS analysis, likely diagenetic in formation from trapped groundwater flow, as this layer abuts an overlaying aquiclude of impermeable mudstone. Above this contact layer is a 50 cm thick grayish orange (Munsell 10YR 7/4) massive mudstone

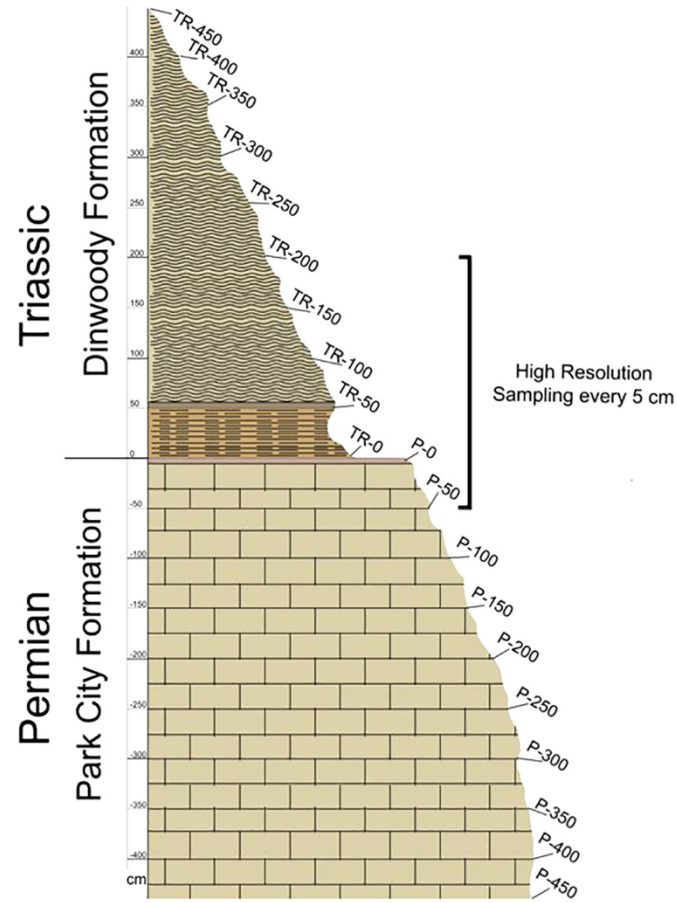

Fig. 2. Stratigraphic column of the entire 9 m measured stratigraphic section across the lithologic contact between the Permian Park City and Triassic Dinwoody Formation, showing high resolution interval where sampling was conducted every 5 cm. Beds currently dip 30° to the north.

(samples TR-0 to TR-45). Lacking sedimentary structures, the mudstone is poorly cemented, and represents the lowest contact layer of the Dinwoody Formation. Starting at 50 cm above the lithologic contact (samples TR-50 and TR-55) is a 10 cm yellowish brown (Munsell 10TR 6/2) siltstone. The final upper zone of the stratigraphic section (samples TR-60 to TR-450) is a yellowish gray (Munsell 5Y 8/1) shale, which features bi-directional cross laminae sedimentary structures (typical of tidal depositional environments), iron oxide concretions, and the cyclic appearance of small (~5 mm) pyrite nodules. Gypsum, either as selenite crystals or druse is found in this upper zone.

2. Methods

2.1. Carbonate analysis

Collected rock samples were crushed and ground to a fine powder in a pestle and mortar, and analyzed utilizing the methodology of Müller and Gastner (1971), which measures pressure of carbon dioxide produced by reaction of carbonate with hydrochloric acid (37%). Samples were calibrated with 2.00 g of pure $CaCO_3$ producing 90 kPa. Rock samples produced between a high of 75 kPa with sample P-15, and a low of 15kPa with sample TR − 105. Resampling resulted in differences of ~3 kPa. Total percent by weight of carbonate in rock samples was calculated from these pressure readings, as well as mass balance using residue of selected samples.

Table 1
Sample descriptions and $CaCO_3$%.

Position (cm)	Sample	Color (Munsell)	Minerals	Sed. Structures	Breakage	Type	$CaCO_3$ kPa	$CaCO_3$% wt.
450	TR-450	5Y 8/1	~10 mm pyrite nodules		Platy	Shale	25	55
350	TR-350	5Y 8/1	~5 mm pyrite nodules		Platy	Shale	34	64
300	TR-300	5Y 8/1	~1 mm pyrite nodules		Blocky	Mudstone	35	65
250	TR − 250	10YR 7/4	Hematite veins		Platy	Shale	24	54
200	TR-200	5Y 8/1		bi-directional cross laminae	Platy	Shale	22	52
195	TR-195	5Y 8/1	~3 mm pyrite nodules	bi-directional cross laminae	Platy	Shale	25	55
190	TR-190	5Y 8/1			Platy	Shale	40	69
185	TR-185	5Y 8/1	~1 mm pyrite nodules		Blocky	Mudstone	30	60
180	TR-180	5Y 8/1			Blocky	Mudstone	30	60
175	TR-175	5Y 8/1		bi-directional cross laminae	Platy	Shale	36	66
170	TR-170	5Y 8/1		bi-directional cross laminae	Platy	Shale	30	60
165	TR-165	5Y 8/1			Blocky	Mudstone	25	55
160	TR-160	5Y 8/1			Platy	Shale	30	60
155	TR-155	5Y 8/1			Platy	Shale	30	60
150	TR-150	5Y 8/1	~5 mm pyrite nodules		Platy	Shale	38	68
145	TR-145	5Y 8/1	~10 mm pyrite nodules		Platy	Shale	30	60
140	TR-140	5Y 8/1	~10 mm pyrite nodules		Platy	Shale	38	68
135	TR-135	5Y 8/1	~1 mm pyrite nodules		Platy	Shale	38	68
130	TR-130	5Y 8/1	Hematite Limonite Gypsum	bi-directional cross laminae	Platy	Shale	30	60
125	TR-125	5Y 8/1			Blocky	Mudstone	20	50
120	TR-120	5Y 8/1	~2 mm pyrite nodules		Blocky	Mudstone	38	68
115	TR-115	5Y 8/1	~3 mm pyrite nodules		Blocky	Mudstone	30	60
110	TR-110	5Y 8/1			Blocky	Mudstone	30	60
105	TR-105	5Y 8/1			Blocky	Mudstone	15	45
100	TR-100	5Y 8/1			Blocky	Mudstone	40	69
95	TR-95	5Y 8/1			Blocky	Mudstone	38	68
90	TR-90	5Y 8/1			Blocky	Mudstone	44	72
85	TR-85	5Y 8/1	Hematite Limonite		Blocky	Mudstone	35	65
80	TR-80	5Y 8/1			Platy	Shale	38	68
75	TR-75	5Y 8/1			Platy	Shale	30	60
70	TR-70	5Y 8/1	~5 mm pyrite nodules		Platy	Shale	35	65
65	TR-65	5Y 8/1			Blocky		27	56
60	TR-60	5Y 8/1		bi-directional cross laminae	Platy	Shale	30	60
55	TR-55	10YR 6/2			Blocky	Mudstone	24	54
50	TR-50	10YR 6/2			Blocky	Mudstone	25	55
45	TR-45	10YR 7/4			Blocky	Mudstone	25	55
40	TR-40	10YR 7/4			Blocky	Mudstone	40	68
35	TR-35	10YR 7/4			Blocky	Mudstone	28	58
30	TR − 30	10YR 7/4			Blocky	Mudstone	25	55
25	TR-25	10YR 7/4			Blocky	Mudstone	35	64
20	TR-20	10YR 7/4			Blocky	Mudstone	30	60
15	TR-15	10YR 7/4			Blocky	Mudstone	42	70
10	TR-10	10YR 7/4			Blocky	Mudstone	49	76
5	TR-5	10YR 7/4			Blocky	Mudstone	32	62
0	TR-0	10YR 7/4			Blocky	Mudstone	20	50
0	P-0	5YR 7/2			Hard	Limestone	40	70
-5	P-5	5Y 8/1	Small specks of Hematite		Hard	Limestone	70	89
-10	P-10	5Y 8/1			Hard	Limestone	65	85
-15	P-15	5Y 8/1			Hard	Limestone	75	94
-20	P-20	5Y 8/1			Hard	Limestone	60	82
-25	P-25	5Y 8/1			Hard	Limestone	66	86
-30	P-30	5Y 8/1			Hard	Limestone	66	86
−35	P-35	5Y 8/1			Hard	Limestone	59	81
−40	P-40	5Y 8/1			Hard	Limestone	52	78
−45	P-45	5Y 8/1			Hard	Limestone	NA	NA
−50	P-50	5Y 8/1			Hard	Limestone	70	88
−150	P-150	5Y 8/1			Hard	Limestone	NA	NA
−250	P-250	5Y 8/1			Hard	Limestone	NA	NA
−350	P-350	5Y 8/1			Hard	Limestone	NA	NA
−450	P-450	5Y 8/1			Hard	Limestone	NA	NA

2.2. Total organic carbon, total carbon, sulfur, and nitrogen analysis

Analysis of powdered rock samples utilized a ThermoFisher Scientific Flash 2000 Element Analyzer (EA) at the Uintah Basin Campus of Utah State University in Vernal, Utah. 20 mg of each prepared powdered rock sample was placed in tin capsules with vanadium oxide. Prepared tin capsules were analyzed by the EA, which combusts samples at high temperature with a flow of oxygen and utilizes a carrier gas of helium. Reruns from the same source of powdered rock produced errors of 9.55% in nitrogen, and 0.25% in total carbon, while rerun of standards (Cystine) produced errors of < 0.01%. Results are reported as total carbon (TC%), sulfur (S%), and nitrogen (N%). To calculate total

Table 2
Results of element analysis (TC%, N%, S%, and TOC%).

Position (cm)	Sample	TC%	N%	S%	TOC%
450	TR-450	2.86	0.0216	0.000	0.015
350	TR-350	2.05	0.0244	0.861	0.020
300	TR-300	2.40	0.0213	2.175	0.037
250	TR-250	2.50	0.0307	0.000	0.113
200	TR-200	2.48	0.0198	0.000	0.306
195	TR-195	3.00	0.0102	2.547	0.045
190	TR-190	3.03	0.0099	0.000	0.175
185	TR-185	2.92	0.0102	0.000	0.563
180	TR-180	4.04	0.0129	0.000	0.046
175	TR-175	5.14	0.0125	0.000	0.611
170	TR-170	4.60	0.0102	0.000	0.414
165	TR-165	5.28	0.0144	0.000	0.016
160	TR-160	4.30	0.0155	0.000	0.211
155	TR-155	3.65	0.0147	0.000	0.757
150	TR-150	3.60	0.0167	0.000	0.240
145	TR-145	3.43	0.0141	0.000	0.387
140	TR-140	3.37	0.0137	0.127	0.026
135	TR-135	3.56	0.0162	0.000	0.029
130	TR-130	3.25	0.0124	0.000	0.035
125	TR-125	3.01	0.0187	0.000	0.024
120	TR-120	3.51	0.0182	0.000	0.260
115	TR-115	3.32	0.0148	0.035	0.064
110	TR-110	3.51	0.0130	0.000	0.220
105	TR-105	3.89	0.0181	0.000	0.053
100	TR-100	3.54	0.0143	0.000	0.027
95	TR-95	4.18	0.0165	0.000	0.026
90	TR-90	4.05	0.0169	0.000	0.029
85	TR-85	3.50	0.0190	0.000	0.024
80	TR-80	3.49	0.0170	0.000	0.030
75	TR-75	3.55	0.0187	0.000	0.021
70	TR-70	2.54	0.0176	0.061	0.023
65	TR-65	3.30	0.0144	0.000	0.018
60	TR-60	3.07	0.0135	0.000	0.025
55	TR − 55	3.22	0.0142	0.000	0.029
50	TR-50	3.10	0.0161	0.000	0.034
45	TR-45	2.60	0.0151	0.000	0.024
40	TR-40	3.25	0.0187	0.000	0.025
35	TR-35	2.98	0.0168	0.000	0.034
30	TR-30	2.93	0.0192	0.000	0.025
25	TR-25	3.18	0.0187	0.000	0.022
20	TR-20	3.28	0.0190	0.000	0.029
15	TR-15	3.30	0.0198	0.000	0.030
10	TR − 10	3.50	0.0189	0.000	0.028
5	TR-5	4.44	0.0200	0.000	0.027
0	TR-0	5.67	0.0153	0.000	0.061
0	P-0	11.29	0.0000	0.000	0.157
-5	P-5	15.23	0.0134	0.000	3.308
-10	P-10	15.52	0.0135	0.000	4.505
−15	P-15	15.30	0.0473	0.000	5.687
−20	P-20	14.58	0.0302	0.000	5.343
−25	P-25	14.51	0.0285	0.000	4.984
−30	P-30	14.63	0.0091	0.000	4.029
−35	P-35	13.84	0.0000	0.000	6.022
−40	P-40	14.34	0.0000	0.000	5.660
−50	P-50	15.52	0.0000	0.000	NA

organic carbon, about 1 g of each prepared powdered rock sample was reacted to 10 ml of 37% HCl for 24 h. Samples where flushed with deionized water, and desiccated at 35 °C. Approximately 10 mg of each prepared sample was placed in tin capsules and analyzed by the EA. Weights were adjusted by taking the measured weight and adding the CaCO3% multiplied by the measured weight, to get the total original weight of the sample. Results of the second analysis are reported as percent of total organic carbon (TOC %) in each rock sample.

2.3. Carbon isotopic analysis of carbonate

Carbon isotopes in the carbonate rock samples were analyzed using a ThermoFisher Scientific Delta V Advantage Isotope Ratio Mass Spectrometer (IRMS) with a Gasbench II Interface housed at the Utah State University Geology Department in Logan, Utah. Powdered rock samples and standards were measured into glass test tubes, with rock samples measured near 0.150 micrograms. Each prepared test tube was evacuated of atmospheric air with helium in an auto-sampler and injected with 1 ml (20 drops) of 100% phosphoric acid. Four samples did not produce consistent enough peaks to be included (TR-180, P-0, P-15and P − 20). Replicates from the same rock source produced precision better than ± 0.43‰ in $\delta^{13}C$ and ± 0.920‰ in $\delta^{18}O$. All isotope data are reported as per mil (‰) relative to Vienna Pee Dee belemnite (VPDB) standard.

2.4. ICP-MS analysis

The Inductively Coupled Plasma Mass Spectrometry (ICP-MS) at the Utah State University Geology Lab in Logan, Utah was used to determine elemental analysis of the 55 powdered rock samples. Measured 0.1000 g of powdered rock was added to plastic vials and flushed with de-ionized water, nitric acid (HNO_3) and hydrofluoric acid (HF) for digestion and heated to evaporation. Each concentrate was then prepared in a solution to determine concentrations of Ti, V, Cr, Mn, Fe, Co, Ni, Cu, Zn, Ga, Rb, Sr, Pd, Ba, La, Ce, Eu, Pt, Pb, and U relative to lab standards. Concentrations of Pd and Pt are semi-quantifiable since those two standards were not used. All other values are fully-quantitative. Measurement error is reported as standard deviation and percent relative to the standard. Each sample was analyzed at least 5 times and averaged. Samples P-5, P-0, TR-0, and TR-5 were analyzed 10 times and averaged.

2.5. Mercury analysis

Powdered samples were mailed to the University of Nevada in Reno in small plastic boxes. To prevent cross contamination on arrival each sample container was carefully cleaned individually using deionized water and Kim-wipes and transferred to a 7.5 ml vial using a metal spatula cleaned with isopropyl alcohol. After this cleaning procedure, the vials with samples were placed in Ziploc bags for temporary storage. Each sample was then analyzed using a Milestone DMA 80. This instrument is used for EPA Method 7473 for Hg in solids and solutions by thermal decomposition, amalgamation, and atomic absorption spectrophotometry. The NIST 2702 inorganic sediment standard was used to set a calibration curve for the Milestone to measure 0–200 ng of Hg. This standard was used at the beginning of each run to verify the machine was on the set calibration curve. This calibration curve was checked with NIST1575a, 2976 s and 2709. The average concentration of Hg for all 55 samples was 0.0054 ppm (ppm). The lowest concentration of Hg was 0.00081 ppm, found in sample TR-190. The highest concentration of Hg was 0.02324 ppm, found in sample TR-5. The coefficient of variance for the triplicate samples ($n = 5$) was 14%. The mean blank concentration for empty sample boats ($n = 15$) was 0.00003ppm. The minimum blank reading was 0.00001 ppm and the maximum was 0.00007 ppm. The NIST 2702 standard had a mean recovery of 99.18%, with a recovery range of 79.72% to 107.68%.

3. Results

Results are summarized in the following section. Table 1 lists observations from the measured stratigraphic section and carbonate analysis.

Samples P-450 through P-0 are characterized as hard resistant limestone, with $CaCO_3$ by % wt. ranging from 78% to 94%. Samples TR-0 to TR-450 are mudstones and shales which contain less $CaCO_3$ by % wt. ranging from 45% to 76%, this difference is statistically significant using Student's *t*-Test probability, $P = .0000000139$, $P < .005$.

Table 2 lists observations from the element analysis, including total carbon, nitrogen, sulfur, and organic carbon % wt, through oxidation at high temperature through a carrier gas of helium.

Table 3
Results of $\delta^{13}C$ and $\delta^{18}O$ in Carbonate Analysis (VPDB).

Position (cm)	Sample	$\delta\ ^{13}C/^{12}C$	stdev	$\delta\ ^{18}O/^{16}O$	stdev	n
450	TR-450	−2.03	0.11	−4.19	0.15	8
350	TR-350	−1.29	0.02	−2.61	0.03	8
300	TR-300	−1.29	0.02	−2.35	0.02	8
250	TR-250	−1.56	0.04	−2.59	0.21	8
200	TR-200	−0.61	0.02	−3.10	0.02	8
195	TR-195	−2.87	0.03	−6.14	0.03	8
190	TR-190	−3.63	0.11	−7.10	0.04	4
185	TR-185	−2.18	0.08	−5.33	0.07	7
175	TR-175	−2.47	0.01	−6.00	0.03	8
170	TR-170	−3.55	0.03	−6.92	0.04	8
165	TR-165	−1.77	0.01	−5.48	0.04	8
160	TR-160	−1.75	0.05	−5.36	0.07	8
155	TR-155	−2.01	0.09	−5.44	0.14	8
150	TR-150	−1.70	0.07	−4.99	0.05	8
145	TR-145	−2.06	0.06	−5.44	0.06	8
140	TR-140	−1.71	0.02	−5.15	0.02	8
135	TR-135	−1.79	0.02	−5.30	0.02	8
130	TR-130	−1.91	0.02	−6.05	0.01	8
125	TR-125	−1.58	0.03	−5.86	0.02	8
120	TR-120	−1.95	0.02	−5.64	0.02	8
115	TR-115	−1.55	0.10	−4.80	0.13	8
110	TR-110	−1.47	0.07	−4.70	0.09	8
105	TR-105	−1.63	0.04	−6.78	0.05	7
100	TR-100	−1.42	0.02	−6.18	0.03	8
95	TR-95	−1.01	0.01	−5.07	0.02	8
90	TR-90	−1.29	0.02	−6.69	0.02	8
85	TR-85	−0.37	0.10	−3.87	0.07	8
80	TR-80	−0.76	0.09	−4.10	0.11	7
75	TR-75	−0.85	0.05	−5.39	0.11	5
70	TR-70	−0.26	0.02	−4.37	0.03	8
65	TR-65	−0.63	0.03	−5.21	0.05	8
60	TR-60	0.01	0.05	−4.60	0.04	8
55	TR-55	−0.14	0.12	−4.41	0.12	8
50	TR-50	0.38	0.05	−4.50	0.07	5
50	TR-50R	0.21	0.05	−4.19	0.07	8
50	TR-50	0.47	0.02	−4.00	0.02	8
45	TR-45	1.03	0.16	−3.38	0.14	8
40	TR-40	0.52	0.05	−3.82	0.13	7
35	TR-35	0.69	0.09	−3.70	0.12	6
30	TR-30	1.05	0.08	−4.18	0.08	7
25	TR-25	1.84	0.03	−4.92	0.08	8
20	TR-20	1.45	0.10	−4.73	0.13	8
15	TR-15	1.68	0.07	−4.09	0.08	8
10	TR-10	2.44	0.02	−3.06	0.03	8
5	TR-5	2.10	0.06	−3.88	0.08	8
5	TR-5R	2.52	0.02	−2.96	0.04	8
0	TR-0	2.20	0.05	−2.61	0.08	8
−5	P-5	1.21	0.03	−0.53	0.03	8
−10	P-10	1.89	0.02	2.74	0.03	8
−25	P-25	1.45	0.03	0.24	0.08	8
−30	P-30	2.86	0.02	3.55	0.01	8
−35	P-35	2.36	0.04	3.62	0.05	8
−40	P-40	0.18	0.03	−3.21	0.04	8
−50	P-50	−0.97	0.04	−1.64	0.03	8

Table 4
Results of mercury analysis (Hg ppm).

Position (cm)	Sample	Hg (ppm)	Hg (ppb)/ TOC%
450	TR-450	0.00143	49.95
350	TR-350	0.00247	120.78
300	TR-300	0.00168	70.06
250	TR-250	0.00115	46.04
200	TR-200	0.00153	61.62
195	TR-195	0.00171	56.98
190	TR-190	0.00081	26.70
185	TR-185	0.00349	119.64
180	TR-180	0.00275	68.07
175	TR-175	0.00117	22.77
170	TR-170	0.00117	25.43
165	TR-165	0.00301	57.03
160	TR-160	0.00262	60.97
155	TR-155	0.00138	37.84
150	TR-150	0.00349	96.89
145	TR-145	0.00483	140.94
140	TR-140	0.00482	143.07
135	TR-135	0.00417	117.00
130	TR-130	0.00156	47.99
125	TR-125	0.00258	85.83
120	TR-120	0.00293	83.45
115	TR-115	0.00142	42.84
110	TR-110	0.00173	49.84
105	TR − 105	0.00216	55.53
100	TR-100	0.00542	153.06
95	TR-95	0.00482	115.20
90	TR-90	0.00217	53.63
85	TR-85	0.00200	57.19
80	TR-80	0.00345	98.94
75	TR-75	0.00263	74.19
70	TR-70	0.01966	775.24
65	TR-65	0.01301	394.48
60	TR-60	0.00588	191.34
55	TR-55	0.00544	169.10
50	TR-50	0.00822	265.08
45	TR-45	0.00585	225.35
40	TR-40	0.00432	132.96
35	TR-35	0.01095	367.82
30	TR-30	0.00437	149.05
25	TR-25	0.00418	131.49
20	TR-20	0.00684	208.47
15	TR − 15	0.00731	221.78
10	TR-10	0.01334	381.36
5	TR-5	0.02324	523.07
0	TR-0	0.02095	369.62
0	P-0	0.01853	164.13
-5	P-5	0.00306	20.09
-10	P-10	0.00594	38.27
-15	P-15	0.01196	78.17
−20	P-20	0.00718	49.25
−25	P-25	0.00694	47.83
−30	P-30	0.00489	33.42
−35	P-35	0.00488	35.26
−40	P-40	0.00274	19.11
−50	P − 50	0.00229	14.76

Samples P-50 through P-0 display high amounts of carbon (TC) % wt. ranging from 15.52% to 11.29%, and exhibit high amounts of total organic carbon (TOC) % wt. from 6.02% to 3.31% before decreasing abruptly with sample P-0 at 0.16%, with samples TR-0 through TR-450 below 0.50%. Nitrogen (N%) levels are not statistically different between samples P-50/P-0 and TR-0/TR-450, $P = .5576$, $P > .05$. Samples TR-70, TR-115, TR-140, TR-195, TR-195, TR-300, TR-350 show elevated sulfur (S%) by wt., which correspond closely to observed pyrite crystals in hand samples (Table 1).

Results from the analysis on the ratios of carbon and oxygen isotopes from powdered rock samples are featured in Table 3.

The results show a decrease in $\delta^{13}C_{carb}$ ratios from a high of 2.89‰ VPDB with sample P-30, to a low of −3.63‰ VPDB with sample TR-190. This indicates that the amount of ^{12}C increased relative to the amount of ^{13}C during the deposition of the sediments. The $\delta\ ^{18}O_{carb}$ values also decreased from a high of 3.62‰ VPDB with sample P-35 to a low of −7.10‰ VPDB with sample TR-190, indicating an increase in ^{16}O relative to ^{18}O during deposition. Samples TR − 50 and TR-5 were replicated from the same rock sample (TR-50R, TR-5R in Table 3), whereas *n* refers to replicates of produced CO_2 which was used to calculate standard deviation in Table 3.

Results from the mercury analysis are presented in Table 4.

Samples show a low of 0.00081 ppm with sample TR-190, and a high of 0.02324 ppm with sample TR-5. The amount of mercury is ten times more than background amounts within the basal 10 cm of the Triassic Dinwoody Formation.

Table 5 lists the results of the ICP-MS analysis of siderophile elements in the rock samples.

Most lithophile elements show an increase across the lithologic

Table 5
Results of ICP-MS Analysis Siderophile Elements (Mn, Fe, Co, Ni, Pd, Pt).

Position (cm)	Sample	^{55}Mn (ppm)	^{56}Fe (ppm)	^{59}Co (ppm)	^{60}Ni (ppm)	^{62}Ni (ppm)	Ni^{Total} (ppm)	^{105}Pd (ppb)	^{195}Pt (ppb)
450	TR-450	423	11,320	6.2	14.2	23.6	126.5	0.0	0.003
350	TR-350	353	23,600	12.3	28.7	39.2	227.5	0.0	0.003
300	TR-300	302	26,890	4.7	19.7	28.9	162.9	0.0	0.004
250	TR-250	279	13,660	3.8	12.6	21.9	115.4	0.0	0.003
200	TR-200	283	9630	3.2	12.6	22.6	118.0	0.0	0.003
195	TR-195	330	11,690	2.8	9.4	14.7	80.9	0.0	0.002
190	TR-190	328	7320	3.2	8.3	13.9	74.1	0.0	0.002
185	TR-185	327	6090	3.0	9.6	16.9	88.7	0.0	0.005
180	TR-180	391	8220	3.2	8.4	15.6	80.2	0.0	0.004
175	TR-175	466	7520	4.3	9.0	14.9	80.1	0.0	0.005
170	TR-170	439	7150	3.9	7.1	13.4	68.7	0.0	0.007
165	TR-165	494	9130	4.6	10.7	16.8	92.2	0.0	0.003
160	TR-160	457	12,550	5.7	16.1	23.8	133.6	0.0	0.003
155	TR-155	414	14,820	5.6	15.0	21.9	123.4	0.0	0.007
150	TR-150	398	30,630	5.9	15.8	22.9	129.7	0.0	0.009
145	TR-145	395	12,400	4.0	10.7	18.2	97.0	0.0	0.007
140	TR-140	418	18,340	4.6	15.1	23.6	129.7	0.0	0.006
135	TR-135	436	14,550	6.2	15.9	22.4	128.5	0.0	0.007
130	TR-130	445	12,350	5.9	16.6	24.2	136.6	0.0	0.006
125	TR-125	400	14,170	5.3	15.3	23.3	129.5	0.0	0.007
120	TR-120	441	14,380	5.5	13.3	21.4	116.2	0.0	0.005
115	TR-115	427	12,380	5.1	16.5	24.5	137.2	0.0	0.006
110	TR-110	405	12,350	4.8	12.8	19.7	109.1	0.0	0.009
105	TR − 105	477	10,240	8.6	17.0	23.8	136.9	0.0	0.007
100	TR-100	426	11,050	5.8	17.9	25.8	146.3	0.0	0.008
95	TR-95	467	12,680	6.2	17.9	26.8	149.7	0.1	0.005
90	TR-90	452	13,000	6.3	17.4	25.4	143.3	0.0	0.011
85	TR-85	454	14,970	7.2	17.0	25.9	143.6	0.0	0.005
80	TR-80	437	16,770	6.6	17.7	27.4	150.9	0.0	0.007
75	TR-75	432	14,810	7.0	16.6	26.4	144.2	0.0	0.005
70	TR-70	409	24,900	9.5	28.2	37.0	218.3	0.0	0.009
65	TR-65	376	14,040	5.9	18.6	26.4	150.8	0.0	0.008
60	TR-60	351	15,120	5.8	21.0	28.5	165.8	0.0	0.009
55	TR-55	384	14,950	6.6	23.4	32.7	188.0	0.3	0.005
50	TR-50	337	10,920	6.8	23.7	32.0	186.6	0.2	0.009
45	TR-45	363	10,560	6.0	15.0	26.3	138.3	0.6	0.008
40	TR-40	397	12,820	7.4	16.0	27.8	146.5	0.9	0.007
35	TR-35	352	11,790	7.8	19.3	29.4	163.0	0.8	0.009
30	TR-30	374	11,300	7.6	20.4	32.0	175.4	0.7	0.008
25	TR-25	385	12,900	9.0	25.0	36.1	204.3	0.8	0.007
20	TR-20	362	11,540	8.5	21.2	30.9	174.5	0.9	0.009
15	TR − 15	383	12,780	8.6	22.0	32.6	182.7	0.8	0.010
10	TR-10	345	10,520	7.5	18.6	26.6	151.3	0.2	0.012
5	TR-5	380	10,560	5.7	12.7	20.6	111.7	1.0	0.015
0	TR-0	459	10,260	5.7	11.9	17.7	99.2	1.5	0.011
0	P-0	1018	57,790	8.0	21.6	19.8	138.7	1.2	0.011
-5	P-5	371	600	0.8	4.8	1.2	20.1	0.7	0.014
-10	P-10	370	1220	1.1	4.6	1.8	21.7	1.0	0.015
-15	P-15	400	1510	1.2	5.8	2.8	28.6	0.9	0.016
−20	P-20	468	2560	0.6	6.6	3.9	35.1	1.5	0.019
−25	P-25	362	2380	1.6	7.2	5.2	41.8	1.0	0.030
−30	P-30	394	2190	1.0	7.0	4.5	38.5	1.2	0.028
−35	P-35	380	2570	1.0	7.4	4.8	40.7	1.3	0.035
−40	P-40	426	1260	1.3	5.3	2.0	24.2	1.0	0.040
−50	P − 50	350	1190	1.1	5.4	2.2	25.6	1.6	0.041

^{105}Pd and ^{195}Pt values are only semi-quantified with high %RSD due to very small concentrations of these elements in the samples and no lab standard utilized.

boundary, with a spike of iron and manganese in sample P-0, with iron at 57,790 ppm and manganese at 1018 ppm, these are three to five times background levels found in other samples. Total nickel increases significantly across the boundary, with the highest value found in sample TR-350 high the section, with a measured 227.5 ppm total amount of nickel. The lowest value of 20.1 ppm was found in sample P-5, just below the lithologic boundary. Both palladium and platinum remain low across the boundary, and don't show any change across the section.

Table 6 lists the results of the ICP-MS analysis of chalcophile elements.

Copper is higher in the lower Park City Formation, with a high of 104.7 ppm in sample P-50. Zinc is high near the lithologic boundary, particularly between samples P-0 and TR-35, the basal 35 cementers of the Dinwoody Formation. Lead is also elevated in this portion of the stratigraphic section.

Table 7 shows the results of the ICP-MS analysis of lithophile elements, that show an increase across the lithological boundary for most element concertations, except for europium, which remains the same and uranium, which declines. Strontium is highly elevated in samples at the boundary. TR-0 and TR-5 are double other measured samples in the Dinwoody Formation, and greater than triple the values measured in samples in the lower Park City Formation.

Table 6
Results of ICP-MS Analysis Chalcophile Elements (Cu, Zn, Ga, Pb).

Position (cm)	Sample	^{65}Cu (ppm)	^{66}Zn (ppm)	^{71}Ga (ppm)	^{208}Pb (ppm)
450	TR-450	14.1	32.6	11.2	1.2
350	TR-350	13.8	69.6	10.7	0.1
300	TR-300	19.3	42.4	8.7	5.5
250	TR-250	11.1	17.5	7.8	4.3
200	TR-200	7.8	36.7	10.6	0.0
195	TR-195	1.6	18.2	4.7	0.0
190	TR-190	2.8	15.0	5.0	0.0
185	TR-185	1.4	8.0	5.1	0.0
180	TR-180	5.2	12.6	6.2	0.7
175	TR-175	3.3	16.2	5.9	0.0
170	TR-170	1.4	15.8	4.8	0.0
165	TR-165	5.4	14.1	6.9	0.0
160	TR-160	5.2	32.1	7.3	0.0
155	TR-155	6.7	39.4	7.4	5.1
150	TR-150	11.8	41.3	8.1	10.9
145	TR-145	4.7	25.0	7.5	4.4
140	TR-140	7.8	40.7	7.3	2.1
135	TR-135	5.5	39.4	7.9	1.3
130	TR-130	6.7	31.1	6.9	5.0
125	TR-125	7.3	30.5	7.5	2.8
120	TR-120	5.4	29.6	9.1	0.0
115	TR-115	5.0	36.6	8.1	0.0
110	TR-110	4.6	26.3	7.8	5.7
105	TR − 105	5.4	21.4	7.9	5.7
100	TR-100	6.7	31.1	7.6	6.7
95	TR-95	4.7	28.0	8.9	2.4
90	TR-90	7.7	33.8	8.6	0.0
85	TR-85	6.1	30.8	9.5	0.2
80	TR-80	8.5	34.4	9.4	8.1
75	TR-75	8.4	31.9	10.9	5.4
70	TR-70	21.6	65.4	9.7	14.8
65	TR-65	10.2	39.3	9.4	9.3
60	TR-60	7.0	42.7	8.7	12.4
55	TR-55	6.1	42.3	9.6	2.8
50	TR-50	6.8	33.8	11.0	8.7
45	TR-45	7.2	46.3	11.2	3.0
40	TR-40	8.2	51.8	13.0	5.7
35	TR-35	9.8	67.7	10.8	5.6
30	TR-30	9.2	78.3	12.1	3.7
25	TR-25	11.3	87.4	12.4	8.9
20	TR-20	11.5	69.4	11.5	6.5
15	TR − 15	13.1	80.0	12.8	11.2
10	TR-10	11.9	59.1	11.4	12.0
5	TR-5	11.2	59.2	11.0	14.7
0	TR-0	6.4	50.6	8.8	5.5
0	P-0	5.8	58.9	1.2	6.3
-5	P-5	6.8	15.5	0.0	0.0
-10	P-10	42.4	22.6	0.1	0.0
-15	P-15	28.5	32.0	0.2	0.0
−20	P-20	30.3	53.0	0.3	0.0
−25	P-25	12.1	50.4	0.7	1.4
−30	P-30	9.0	50.0	0.2	0.0
−35	P-35	15.7	56.9	0.5	0.0
−40	P-40	10.7	28.9	0.3	0.0
−50	P − 50	104.7	19.9	0.1	0.0

4. Discussion

4.1. Discussion of the carbonate analysis

The observed $CaCO_3$ content of the rock by weight decreases across the lithologic contact (between samples P-0 and TR-0) from a range of 78–94% to a low of 50–72% by weight (Fig. 3; Table 1) is consistent with an abrupt shoaling of the CCD due to acidification of the ocean by the absorption of high levels of atmospheric CO_2 (Zachos et al., 2005). This indicates that atmospheric CO_2 was abruptly elevated during the period of deposition of the rock layers.

4.2. Discussion of the total organic carbon, total carbon, sulfur, and nitrogen analysis

Total Organic Carbon (TOC %) content of the rocks shows an abrupt shift from an average of 4.89% to an average of 0.12% by weight across the lithologic contact (Fig. 4, Table 2) is interpreted as a significant loss of bioproductivity across this interval, and together with observed sedimentary structures it suggests that sea level remained within the photic zone and upper shoreface throughout the stratigraphic section. The major lithologic shift at the contact between samples P-0 and TR-0 is most-likely due to the effects of the extinction event, with decreased input of both $CaCO_3$ and TOC in the lower-most Dinwoody Formation rather than eustatic change.

Analysis of the sulfur content (S %) of the rock layers shows a cyclic appearance of high levels of sulfur likely driven by the presence of pyrite (Figs. 5 & 6) beginning with sample TR-70, 70 cm above the lithologic contact (Figs. 5 & 6, Table 2). Presence of pyrite has been documented from other Permian-Triassic sections (Wignall and Hallam, 1992; Wignall et al., 2005; Kakuwa, 2008; Shen et al., 2007; Bond and Wignall, 2010; Tian et al., 2014; Liao et al., 2017; Huang et al., 2019) and is indicative of widespread anoxic ocean waters following the Permian-Triassic event (Isozaki, 1997; Grice et al., 2005; Song et al., 2012). The presence of pyrite within the bi-directional cross laminae strata of the upper zone indicates that a severe anoxia of the upper shoreface followed the initial extinction event in Utah. Pyrite crystals appear to have been deposited cyclically, alternating between oxygenated and deoxygenated waters, with the highest concentration of sulfur in sample TR-195195 cm above the contact. Pyrite crystals are found widely distributed in these thinly bedded laminated shales and are non-sorted.

This pyrite may have formed at depth and been redeposited (Kershaw et al., 2018), but the presence of pyrite (even as clasts) indicates low dissolved oxygen content in these shallow marine waters. Pyrite crystals are common in the lower Dinwoody Formation, but are not found within the lower-most mudstone (TR-0 to TR-45). These samples (TR-0 to TR-45) contain low levels of sulfur, indicating a delay between the onset of ocean acidification and the onset of anoxia of 70 cm in the local section (Fig. 6).

4.3. Discussion of the carbon isotopic analysis of carbonate

Carbon isotopic analysis ($\delta^{13}C$) of carbonate shows an overall decline in $\Delta^{13}C/^{12}C$ ratios from a high of 2.59‰ VPDB 30 cm below the lithologic contact to a low of −3.63‰VPDB at 190 cm above the contact, similar to changes observed elsewhere at the Permian-Triassic boundary in shallow marine settings (Magaritz et al., 1988; Baud et al., 1989; Berner, 2002; Benton and Twitchett, 2003; Payne et al., 2004; Korte et al., 2004; Krull et al., 2004; Korte and Kozur, 2010; Luo et al., 2010; Meyer et al., 2011; Sun et al., 2012; Song et al., 2013; Meyer et al., 2013; Liu et al., 2017) (Fig. 7, Table 3). In comparison to the GSSP section in Meishan, China, the observed gradual decrease in carbonate $\delta^{13}C$ values in Utah closely matches that observed between beds 24 to 28 in China (Xie et al., 2007; Luo et al., 2010) during the greatest extinction of foraminifera (Song et al., 2009) and is remarkably similar to shallow marine environments along the south China craton (Sun et al., 2012; Song et al., 2013). The rate of carbon isotopic decrease is about 0.15 ‰ per 5 cm, indicating a gradual negative shift in carbon isotopic ratios ($\delta^{13}C$) over 200 cm in the lower Dinwoody Formation. $\delta^{13}C$ values remain low (sample TR-450 = −2.03‰ VPDB) up to the top of the measured 9-m section in the lower Dinwoody Formation (Fig. 7). The cause of this isotopic shift is due to the enrichment of ^{12}C in the carbon cycle during the deposition of these sediments. With slightly less atomic mass, ^{12}C is more abundant in organic carbon sources, where lighter carbon is preferentially bonded to hydrogen. The decrease in the $\delta^{13}C$ ratio is consistent with high levels of ^{12}C-rich hydrocarbon emission associated with organic rather than inorganic

Table 7
Results of ICP-MS Analysis Lithophile Elements (Ti, V, Cr, Rb, Sr, Ba, La, Ce, Eu, U).

Pos. (cm)	Sample	^{47}Ti (ppm)	^{51}V (ppm)	^{52}Cr (ppm)	^{85}Rb (ppm)	^{88}Sr (ppm)	^{137}Ba (ppm)	^{139}La (ppm)	^{140}Ce (ppm)	^{153}Eu (ppm)	^{238}U (ppm)
450	TR-450	2230	55	34	69	185	277	22	45	0.9	2.4
350	TR-350	2460	53	40	63	185	278	25	52	0.9	2.6
300	TR-300	2280	43	34	47	172	494	20	41	0.9	2.0
250	TR-250	2240	45	30	43	200	374	19	39	0.8	2.2
200	TR-200	2420	48	37	57	286	318	22	43	0.9	2.1
195	TR-195	1380	28	16	29	208	648	15	30	0.7	1.4
190	TR-190	1430	35	17	31	175	753	12	25	0.7	1.5
185	TR-185	1840	27	19	32	172	283	15	29	0.6	1.7
180	TR-180	1800	34	22	36	180	315	14	27	0.7	1.6
175	TR-175	1710	36	24	34	336	557	19	41	1.0	2.0
170	TR-170	1740	32	21	28	334	997	20	43	1.1	2.0
165	TR-165	1780	40	31	41	263	255	16	32	0.8	1.8
160	TR-160	2030	38	27	43	194	291	15	30	0.7	1.8
155	TR-155	1990	35	27	44	193	312	16	33	0.7	1.9
150	TR-150	1980	36	28	47	193	395	16	34	0.7	2.0
145	TR-145	2110	34	26	42	184	547	18	37	0.8	2.0
140	TR-140	2090	35	27	41	170	371	15	30	0.7	1.9
135	TR-135	2110	37	29	44	185	335	15	32	0.7	2.0
130	TR-130	2090	35	52	41	173	329	14	29	0.7	1.9
125	TR-125	2120	39	28	45	179	303	15	31	0.7	1.9
120	TR-120	2240	43	34	52	233	776	18	37	0.9	2.1
115	TR-115	2260	40	35	47	197	344	16	34	0.7	2.0
110	TR-110	2120	38	29	47	198	304	19	39	0.8	2.1
105	TR − 105	2170	40	28	47	203	377	19	39	0.8	2.1
100	TR-100	2260	40	30	44	209	360	19	40	0.8	2.2
95	TR-95	2330	48	34	51	240	359	20	42	0.9	2.2
90	TR-90	2210	47	33	50	230	312	18	36	0.8	2.1
85	TR-85	2400	52	35	56	234	309	19	39	0.8	2.3
80	TR-80	2560	51	35	55	225	358	19	39	0.8	2.5
75	TR-75	2680	58	40	63	253	547	22	45	0.9	2.5
70	TR-70	2540	53	37	57	213	451	19	37	0.8	2.6
65	TR-65	2400	50	34	56	213	344	21	43	0.9	2.5
60	TR-60	2280	49	31	51	211	375	20	40	0.8	2.5
55	TR-55	2490	56	36	57	237	345	20	41	0.9	2.6
50	TR-50	2430	62	39	66	294	318	24	50	1.0	2.9
45	TR-45	3010	57	43	67	286	311	24	47	0.9	3.2
40	TR-40	3080	67	48	77	302	308	25	48	0.9	3.3
35	TR-35	2730	52	40	64	261	284	20	39	0.8	3.0
30	TR-30	3070	58	46	73	291	315	22	42	0.9	3.3
25	TR-25	3060	61	47	74	325	295	22	41	0.9	3.5
20	TR-20	2790	57	44	69	305	269	20	38	0.8	3.3
15	TR − 15	3010	64	50	77	326	290	21	40	0.8	3.5
10	TR-10	2640	55	42	68	390	275	21	40	0.8	3.3
5	TR-5	2480	55	46	64	615	250	24	48	1.0	3.7
0	TR-0	1830	46	42	50	617	201	22	45	1.2	3.6
0	P-0	120	7	15	4	210	116	13	29	1.0	4.1
-5	P-5	20	3	10	1	132	7	4	1	0.1	6.6
-10	P-10	40	7	18	1	162	3	6	2	0.2	2.9
-15	P-15	40	13	18	1	149	1	5	1	0.1	3.5
−20	P-20	80	9	43	2	111	0	12	4	0.4	5.6
−25	P-25	120	8	32	3	127	4	9	4	0.3	6.5
−30	P-30	60	8	35	2	106	0	7	2	0.2	4.6
−35	P-35	80	7	40	2	123	0	9	3	0.3	5.8
−40	P-40	40	5	16	1	98	0	4	1	0.1	17.8
−50	P-50	30	11	19	1	122	1	5	1	0.1	3.1

sources.

4.4. Discussion of the nitrogen from EA analysis and copper from ICP-MS analysis as a method for temporal astrological calibration

Results from the nitrogen (N) and copper (Cu) analysis offer a mechanism to temporally calibrate the stratigraphic section (Fig. 8, Tables 2 and 6). Samples collected in the Park City Limestone show erratic N content, likely due to the heterogeneous nature of porous limestone, but N content from the mudstone/shale samples TR-0 to TR-200 show three rhythmic cycles of increasing and decreasing nitrogen values indicative of precession cycles (~23 ky, Hays et al., 1976; Straub et al., 2013) in Earth's Milankovitch orbital variation. A similar cyclic pattern is observed in Cu obtained from ICP-MS analysis of rock samples (Fig. 8). Computer simulations of the Permian-Triassic ocean system show strong influence of precession orbital cycles on nutrient cycles, which would include temperature-dependent N levels and Cu input from variability in river discharge (Winguth and Winguth, 2013).

A ~69,000-year estimate for the length of time for the deposition of sediment between level TR-0 to TR-200 was determined from the orbital cyclicity of the nitrogen and copper observed in the stratigraphic section that show 3-possible orbital precession cycles (Fig. 8). The data implies that the duration of time between the onset of shallow ocean acidification and anoxia is estimated at ~23,000 years (TR-0 to TR-70). Sedimentation rates based on modern equivalent depositional environments (0.5 to 2.0 mm/year from a study in a protected bay in the Baltic Sea (Szmytkiewicz and Zalewska, 2014)) suggest a shorter duration of 1400 to 350 years between acidification and anoxia, but sedimentation rates likely slowed after the onset of acidification, and the longer duration is more likely.

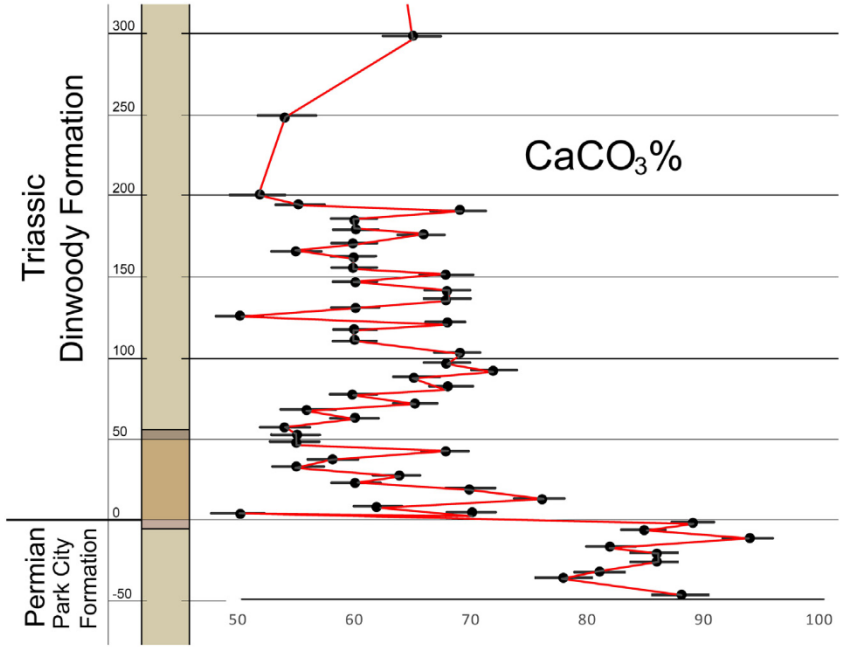

Fig. 3. Percent by weight of $CaCO_3$ in collected rock samples (Table 1). Standard deviation 4.0 shown in error bars.

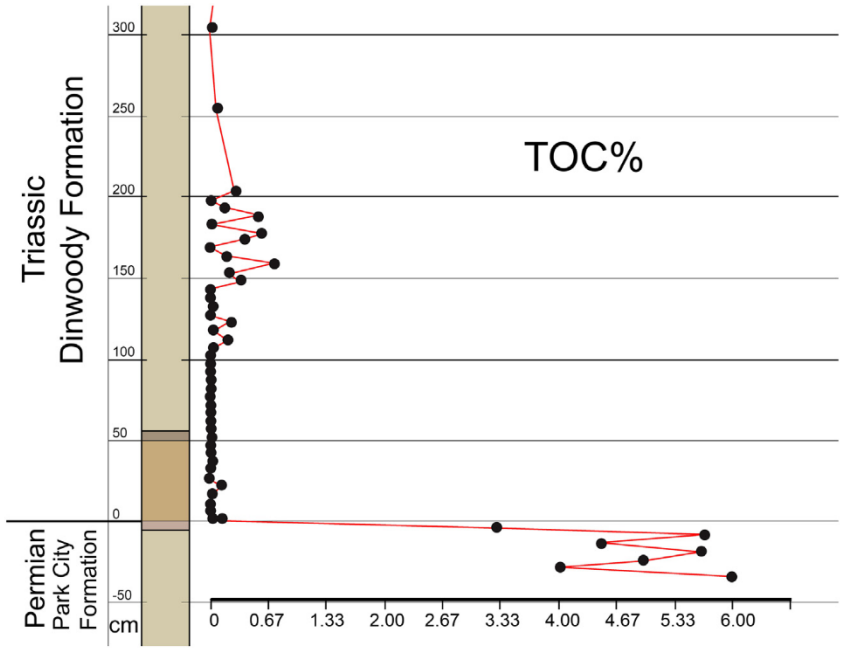

Fig. 4. Percent by weight of Total Organic Carbon (TOC) in collected rock samples (table S2). Standard deviation 0.39 for Park City samples, 0.007 for Dinwoody samples.

Matching the δ13C negative excursion in Utah with the GSSP section in Meishan, China (Fig. 7) allows for direct comparison between the two stratigraphic sections. In the Meishan section zircons have been dated from two beds (beds 25 and 28) within the δ13C negative excursion, indicating a duration of ~61,000 years (Burgess et al., 2014), or range between 13,000 to 109,000 years (Baresel et al., 2017) for the major δ13C negative shift (Shen et al., 2011). The stratigraphic beds corresponding to the same interval in Utah indicate a similar duration of ~69,000 years. Shen et al. (2018) estimated a duration of the mass extinction event in South China's thicker Penglaitan section as < 62,000 years, with sedimentation rates slowing across the boundary from 0.69 mm/y to 0.22 mm/y. These estimates are similar to the study by Rampino et al. (2000) which used patterns of orbital cyclicity in the Austrian Alps to estimate that the onset of the event took place around 30,000 to 40,000 years.

4.5. Discussion of mercury analysis

Analysis of the 55 rock samples for Hg content demonstrates a Hg enriched zone within the first 70 cm above the lithologic contact (Fig. 9, Table 4). Two spikes in Hg were found at 5 cm (0.02324 ppm) and 70 cm (0.01966 ppm) above the contact, with background levels below 0.01 ppm. The results indicate a 2-to-4 fold increase in Hg across the boundary. The high Hg content suggests a fallout of atmospheric ash from coal combustion (Grasby et al., 2011; Sanei et al., 2012; Grasby et al., 2016; Grasby et al., 2017; Wang et al., 2018), coinciding with the

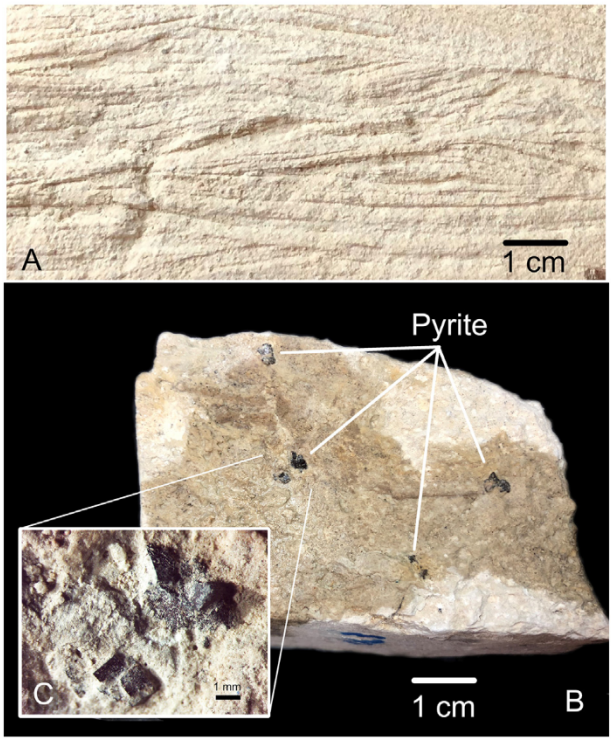

Fig. 5. Cross stratification typical of the lower Dinwoody Formation. B. Observed pyrite on surface of stratigraphic level bedding plane of TR-140. C. Microscope magnification of pyrite show in B.

lithologic shift due to the acidification of ocean water, and with the onset of euxinic ocean water that occurs at 70 cm above the lithologic contact with the first appearance of pyrite. Mercury is found in coal due to the fact that Hg is assimilated by vegetation. Specifically, Hg is taken up by way of the stomata and cuticle, and in trees it is translocated to and stored in tree rings (Arnold et al., 2017). Sanei et al. (2012) hypothesized that Hg drawdown after the P-T event was a result of sulfide-Hg interactions from the onset of euxinic ocean water conditions. Indeed, these results from Utah support that assertion, as Hg levels decrease only after the first appearance of pyrite in the local stratigraphic section (Fig. 6; Fig. 9).

4.6. Discussion of ICP-MS analysis

Analysis of the 55 rock samples utilizing an ICP-MS demonstrates only slightly elevated Ni content within the first 70 cm above the lithologic contact (Fig. 10, Table 5). Combined ^{60}Ni and ^{62}Ni peak at 65.2 ppm at 70 cm and 61.0 ppm at 25 cm above the contact. Total Ni content ranges from 20 to 200 ppm, below high levels (~250 ppm) reported by Rampino et al. (2017), but within the 80 ppm reported by Kaiho et al. (2001) within the Meishan Section in China. While Ni appears to be enriched within the boundary zone, the amount is not significant enough to implicate a volcanic source (Rampino et al., 2017). Nickel content in terrestrial soils becomes more mobile when exposed to lower pH water (Iyaka, 2011), and this slight enrichment of Ni may be from terrestrial runoff due to more acidic rainwater during the event (Sheldon, 2006).

Zn on the other hand (Fig. 11, Table 6), shows a more significant spike within the boundary interval, similar to results found by Liu et al. (2017) within the Meishan Section in China. In Utah, Zn peaks at 25 cm above the lithologic boundary to 87.4 ppm, while Liu et al. (2017) report Zn peaking just above 100 ppm in bed 24 of the Meishan Section, which, based on comparison of carbon isotopes, is correlative.

Strontium (Sr) levels show a 3-fold increase in samples TR-0 and TR-5 from a background average of 213 ppm to a peak of 617 ppm just above the contact (Fig. 12, Table 7). Lead (Pb) shows an elevated zone with values up to 14 ppm near the contact (Samples TR-5 to TR-15), but also some additional spikes above 10 ppm coinciding with pyrite-rich horizons, at TR-150 and TR-70 (Fig. 13).

Lithology appears to have an effect on most trace elements observed in the stratigraphic column, due to a reduction in sedimentation rates. Mudstone/siltstone layers are enriched in Ti, V, Fe, Co, Ni, Ga, Rb, Ba, La, Ce, Eu, and Pb, while limestone layers are enriched in Cu. Cu, Fe, Ba, and Mn are slightly depleted in the zone between TR-0 to TR-70, with a slight enrichment in Ti, V, Cr, Co, Ga, and Rb in this boundary zone, when compared to other mudstone/siltstone samples (Tables 5-7).

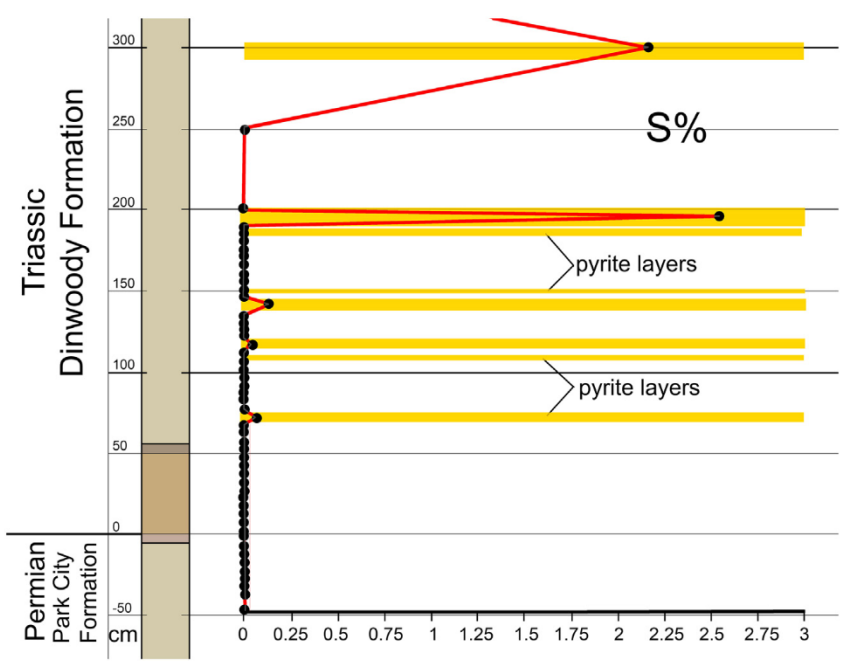

Fig. 6. Percent by weight of sulfur (S) in collected rock samples. Yellow lines indicate observed pyrite crystals in hand samples (Tables 1 and 2). Standard deviation 0.017. (For interpretation of the references to color in this figure legend, the reader is referred to the web version of this article.)

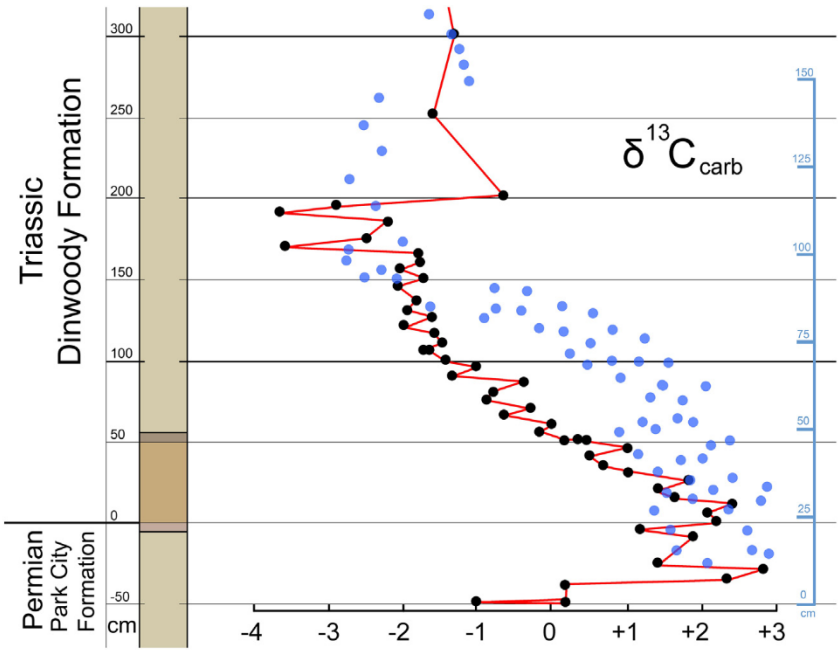

Fig. 7. Carbon isotope ratios of carbonate in collected rock samples. Values are in VPDB (‰). Light blue dots are the observed $\delta^{13}C$ values reported from the GSSP in Meishan China from beds 24 to 28 (Luo et al., 2010), with an estimated thickness of 1.5 m. (Table 3). Standard deviation of standards are between 0.03 and 0.07 and standard deviations for replicates of each sample are between 0.01 and 0.16. (For interpretation of the references to color in this figure legend, the reader is referred to the web version of this article.)

Observed amounts of barium (Ba) between TR-0 and TR-70 show an increase up to 450 ppm (Fig. 14, Table 7). However, in the anoxic upper zone (TR-70 to TR-195), Ba spikes several times, with the highest values (997.2 ppm) found in sample TR-170 (Fig. 14). These high-Ba spikes closely match the sulfur-enriched pyrite framboid horizons (Fig. 6).

Rare elements La, Ce, and Eu, and Pd, Pt, and U show little difference stratigraphically across the boundary. Anomalous high values of siderophile and chalcophile elements (Pt, Pd, Cr, Co, Ni, and Zn) are indicative of extraterrestrial impact events, such as the one discovered at the end of the Mesozoic (Alvarez et al., 1980). Measured levels of these elements observed in the rock layers examined at the Permian-Triassic boundary in Utah remain well below anomalous high values reported from the Cretaceous-Paleogene boundary (Alvarez et al., 1980; Kyte et al., 1985) (Fig. 15, Tables 5-7). There is no evidence in the observed concentrations of siderophile and chalcophile elements in Utah for an extraterrestrial impact at the Permian-Triassic boundary (Fig. 15).

5. Conclusions

This study is the first to examine the Permian-Triassic boundary from a shallow marine setting along the western coastline of Pangea. Previous studies of sediments deposited in shallow marine environments during the Permian-Triassic extinction have principally come from Asia, particularly within deposits representing the Paleo-Tethys Ocean and far eastern coastline of the Panthalassa Ocean (Wignall and Twitchett, 2002). Assessing similarities and differences between the newly discovered section in Utah, and those in Asia, offers a unique

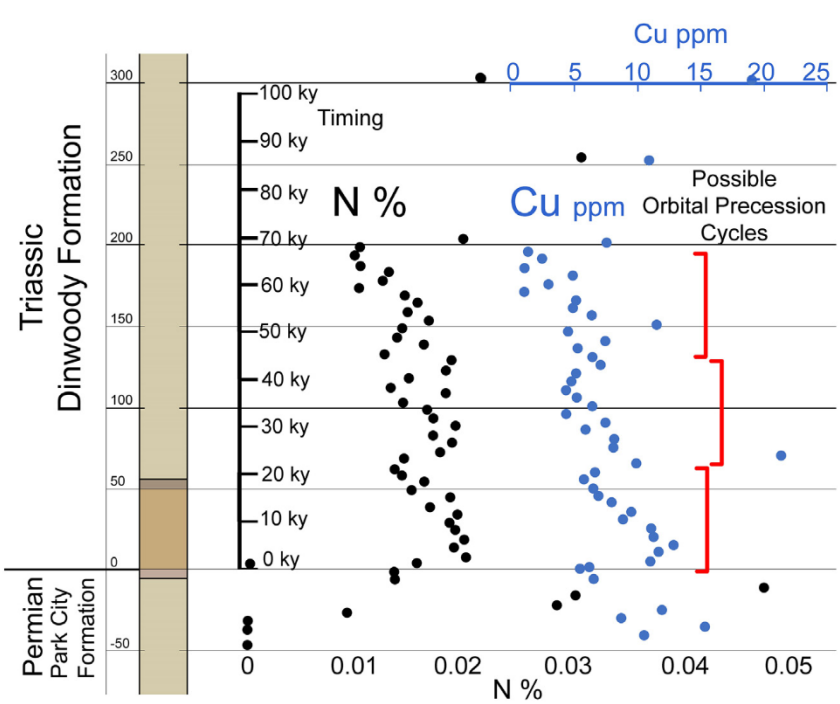

Fig. 8. Percent by weight of nitrogen (N) and parts per million (ppm) of copper (Cu) in collected rock samples. Cyclic variation in N % and Cu (ppm) in the early Dinwoody Formation shows three possible orbital precession cycles in the section, suggesting a temporal scale of ~69,000 years between TR-0 and TR-200 (Tables 2 and 6). N standard deviation 0.002, Cu 0.2.

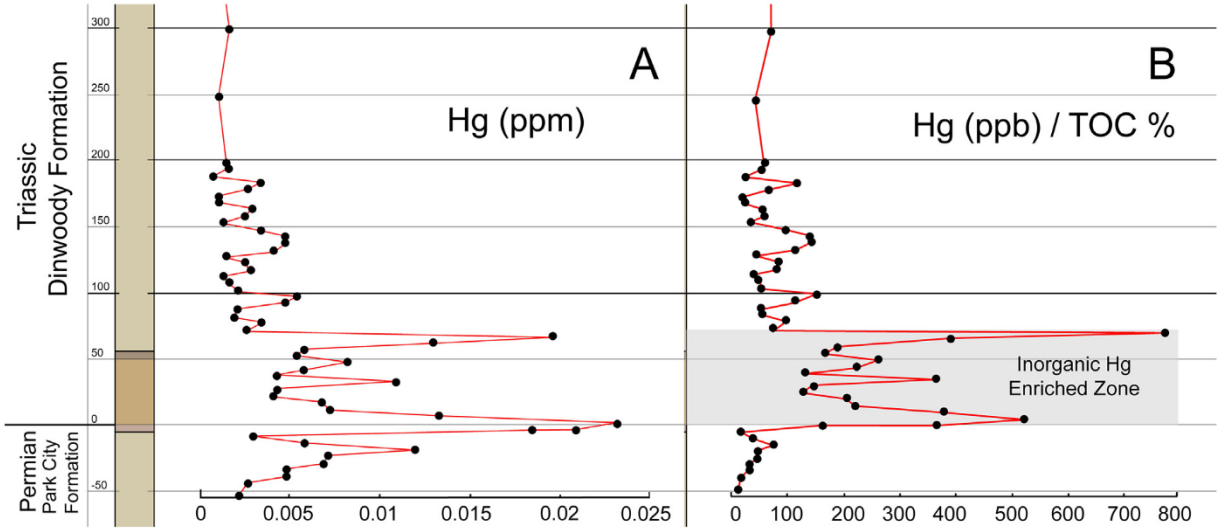

Fig. 9. Measured Hg concentrations in collected rock samples. (A) Hg concentrations in parts per million (ppm), and (B) ratio of Hg compared to measured TOC % showing an enriched inorganic zone from TR-0 to TR-70 (Table 4).

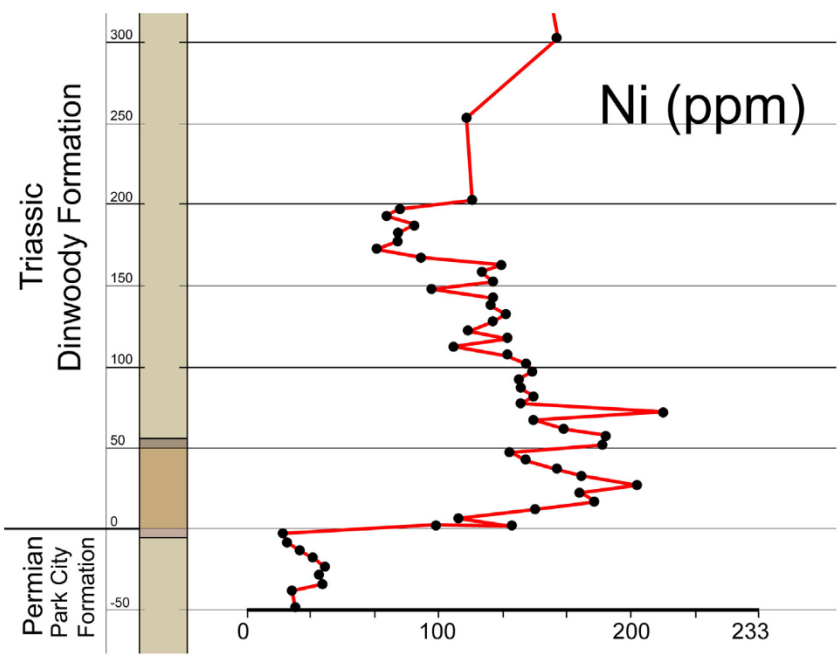

Fig. 10. Measured Ni concentrations (ppm) in collected rock samples. Concentrations are elevated in the Dinwoody Formation due to enhanced chemical weathering from terrigenous sources, but values are well below high-levels (> 250 ppm; Rampino et al., 2017) expected in volcanic ash or extraterrestrial impact events (Table 5). Standard deviation 3.6.

view into the changing chemistry of the Panthalassa Ocean as a whole, which covered as much as 75% of the Earth's surface during this time. Measured values of siderophile and chalcophile element concentrations in Utah demonstrate a lack of evidence for an extraterrestrial impact event at the Permian-Triassic boundary, which is consistent with observations at other boundary sections (Xu et al., 2007; Brookfield et al., 2010).

Recent research has focused on the Siberian Traps large volcanic province as the trigger for the Permian-Triassic event, due in large part to the well constrained dates from the basalt fields, which tie these eruptions temporally within the boundary interval (Renne and Basu, 1991; Renne et al., 1995; Mundil et al., 2004; Payne et al., 2004; Reichow et al., 2009; Burgess et al., 2014; Burgess et al., 2017; Latyshev et al., 2018). Estimates of the total amount of carbon dioxide emitted from these large volcanic provinces (440 to 13,000 gigatonnes of CO_2, Leavitt, 1982; Berner, 2002), was likely alone not enough to push the entire Panthalassa Ocean into the acidic conditions necessary to lead to the observed reduction in shallow marine carbonate deposition in the stratigraphic sections of both Asia and Utah. Volcanic basalts from the Siberian Traps eruptions, however, overlay coal-bearing sedimentary rocks (Reichow et al., 2009). Ogden and Sleep (2012) advanced the idea that the Siberian Traps volcanic providence spread into a regional sill complex, which ignited coal deposits during a second stage of volcanic activity starting at 251.9 million years ago (Burgess et al., 2017). Recently, evidence from the Tunguska Basin north of Irkutsk, Russia demonstrates a vast network of sill intrusions into hydrocarbon rich sedimentary rocks, enough to release an estimated 100,000 gigatonnes of CO_2 (Svensen et al., 2009). Such a scenario would have significantly increased the total carbon dioxide output, enough to acidify the Panthalassa Ocean, then volcanic activity alone. The combustion of large quantities of coal releases significantly larger amounts of carbon dioxide, but also sulfur, Hg, Zn, Pb, and Sr that differ geochemically from volcanic ash.

Atmospheric Hg bio-accumulates in plant tissues (Gustin et al., 2008), which become sequestered in the formation of coal. When coal is combusted this Hg is released back into the atmosphere, where it can be

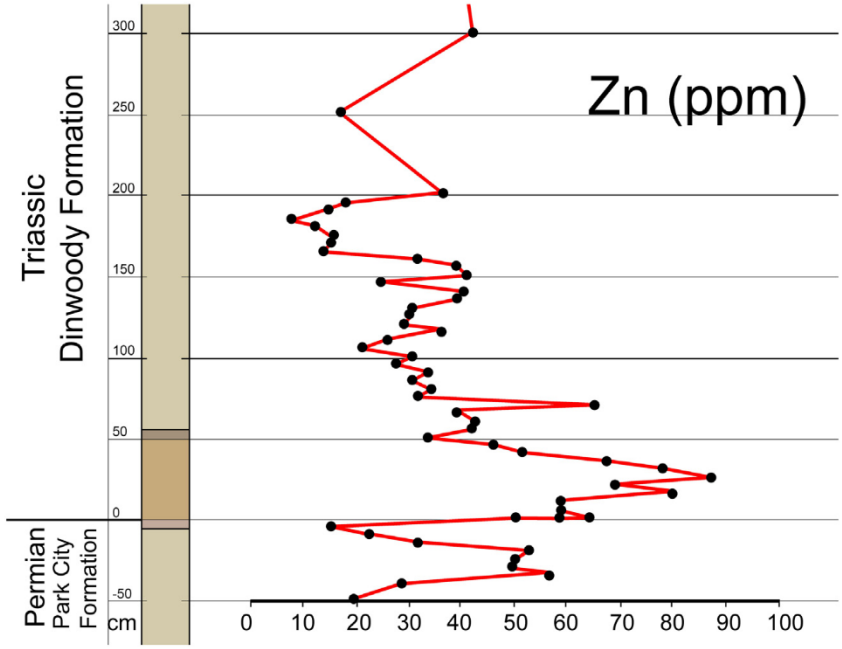

Fig. 11. Measured Zn concentrations (ppm) in collected rock samples from ICP-MS analysis. Values peak within the boundary section at sample TR-25 at 87.4 ppm. Values are well below high-levels (> 300 ppm) expected with an extraterrestrial impact event (Table 6). Standard deviation 3.5.

observed as fallout in soils and sediments. The observed enriched zone of Hg (0–70 cm) within the Permian-Triassic boundary section in Utah supports the idea of coal combustion as the initial driver of the Permian-Triassic extinction, rather than volcanic activity alone. Elevated levels of Zn (above 60 ppm) were also found in the basal 70 cm of the boundary section, which further supports the influence of coal emissions during this time. Coal ash contains higher levels of Zn (55 to 1300 ppm; Doughten, 1997; Briggs, 1997) due to the element's role as a micronutrient in plant tissue, when compared to low Zn levels in volcanic ash (0 to 92 ppm; Taylor and Lichte, 1980; Smichowski et al., 2003). Reported values of δ^{66}Zn from the Permian-Triassic boundary in China (+0.35‰; Liu et al., 2017) are within the range of observed coal ash δ^{66}Zn (+0.26‰ to +0.64%; Ochoa-González and Weiss, 2015). The basal 5 cm of the boundary section in Utah also show an anomalous doubling of Sr (up to 617.2 ppm). Sr is typically found at higher levels in coal (190 to 2100 ppm; Doughten, 1997; Briggs, 1997) compared to volcanic ash (345 to 567 ppm; Taylor and Lichte, 1980). Observed elevated levels of Sr in this basal 5 cm zone may also be due to an increased input from terrestrial sources due to increased chemical weathering, as paleosols across the Permian-Triassic boundary in South Africa show a depletion in Sr levels (Sheldon, 2006), resulting in elevated input in marine sediments from this enhanced weathering. Emissions from burning coal contribute to higher levels of Pb in the atmosphere (Natusch et al., 1974; Block and Dams, 1975). Measured

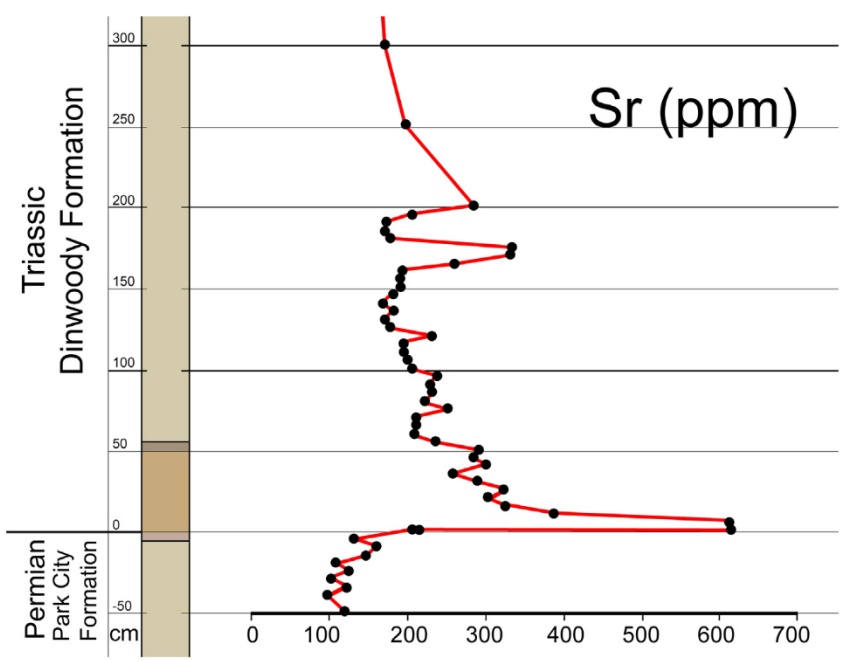

Fig. 12. Measured strontium (Sr) concentrations (ppm) in collected rock samples from ICP-MS analysis. Values peak at the base of the boundary section with sample TR-0 = 618 ppm and TR-5 = 615 ppm (Table 7). Standard deviation 4.6.

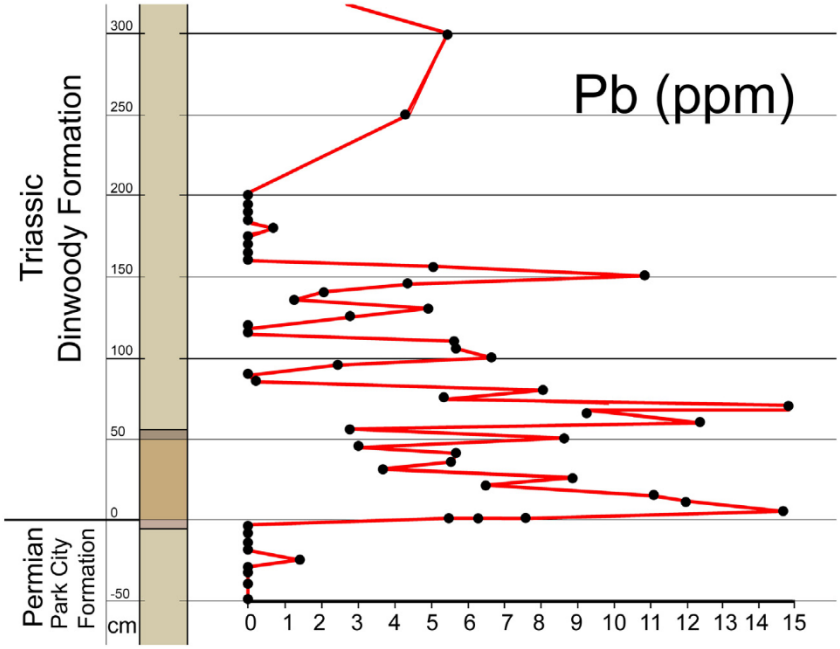

Fig. 13. Measured lead (Pb) concentrations (ppm) in collected rock samples from ICP-MS analysis. Pb is elevated in the lower Dinwoody Formation, especially within the lower boundary section (Table 6). Standard deviation.

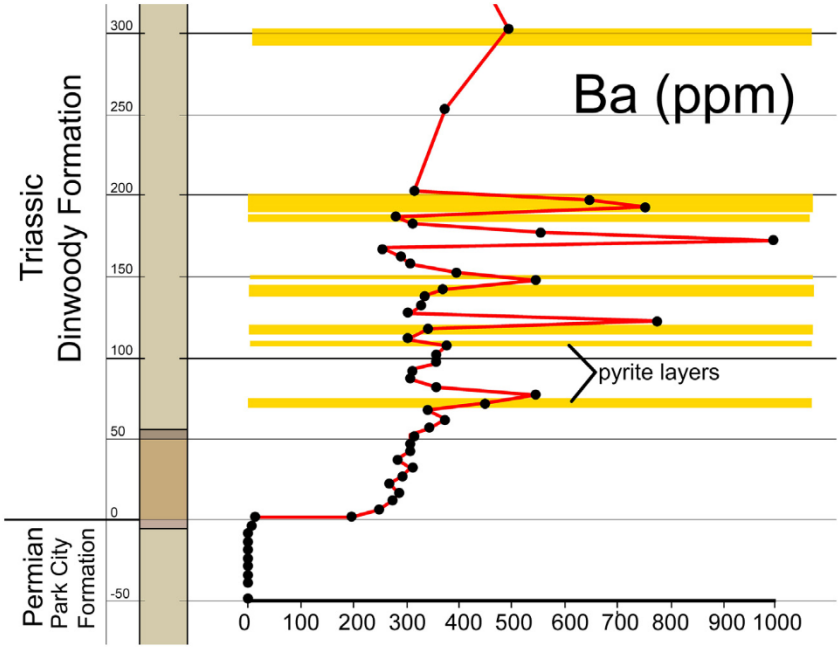

Fig. 14. Measured barium (Ba) concentrations (ppm) in collected rock samples from ICP-MS analysis. Ba is elevated in the observed pyrite framboid layers (Table 7). Standard deviation 3.2.

amounts of Pb in the Utah section show an enriched Pb-layer between samples TR-0 to TR-155, suggesting continued coal emission throughout this time and coinciding with the observed negative carbon isotope excursion.

The elevated levels of Hg, Zn, Sr, and Pb within the 70 cm basal zone of the Permian-Triassic boundary in Utah support coal combustion as the trigger for the initial change in pH chemistry within the Panthalassa Ocean, rather than volcanic activity alone. The lack of any observed volcanic ash in the Utah section contrasts with sections in Asia which record a number of volcanic ash layers near the Permian-Triassic boundary (Lehrmann et al., 2003; Rampino et al., 2017), attributed to eruptions of the nearby Siberian Traps volcanic province. While these eruptions were major events, the distribution of volcanic ash from these eruptions was not global, as it appears that volcanic ash did not reach the far western coastline of Pangea, represented by present-day Utah.

Combustion of subterranean petroleum reservoirs associated with Siberian Traps volcanism could also account for the high levels of Hg, especially if these reservoirs were enriched in the mineral calomel. Heating experiments of Cambrian petroleum-bearing evaporitic rocks associated with contact metamorphism by the Siberian Traps sill complex also exhibit elevated chloride, fluoride, and bromide (Svensen et al., 2009; Black et al., 2012), which were not examined in this study. Beerling et al. (2007) theorized high input of atmospheric chloride (as CH_3Cl) was necessary to deplete the ozone layer enough to explain

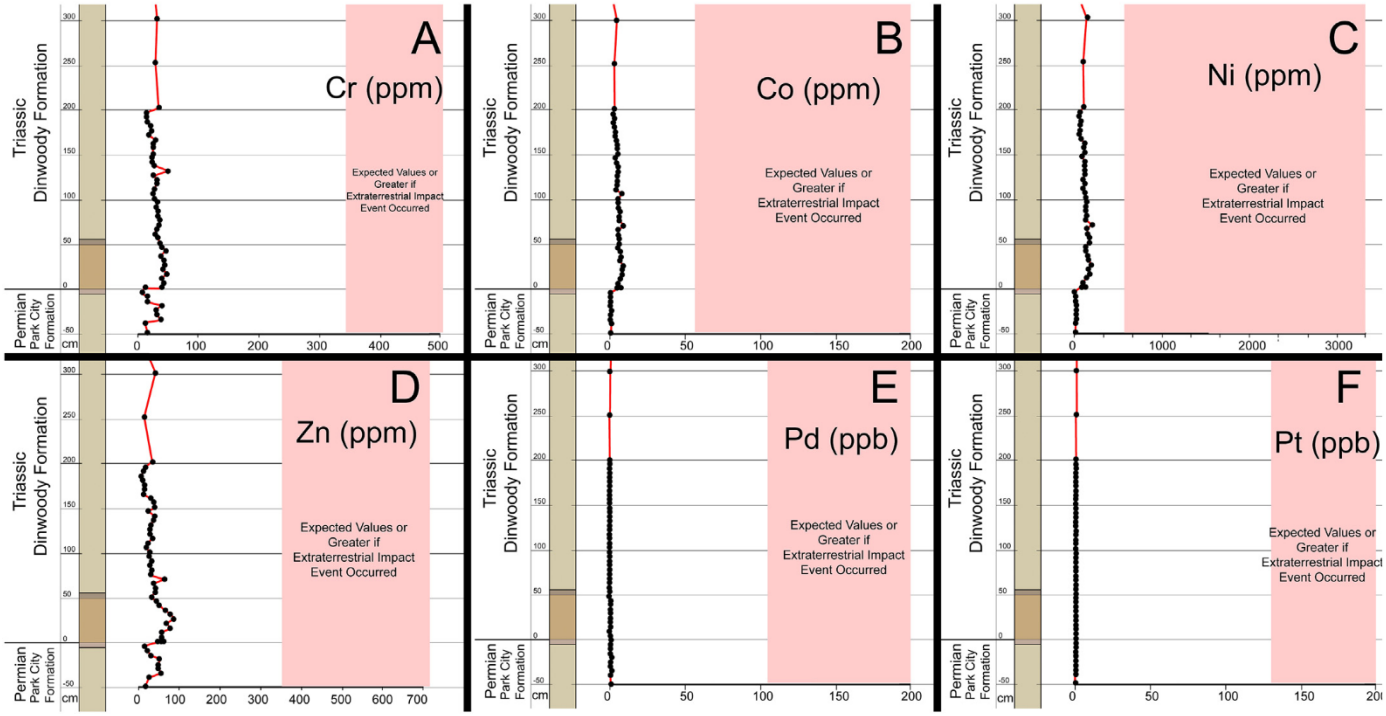

Fig. 15. Measured concentrations of elements (A) Chromium, (B) Cobalt, (C) Nickel, (D) Zinc, (E) Palladium, (F) and Platinum in collected rock samples from ICP-MS analysis compared with concentrations observed across the Mesozoic-Cenozoic boundary sections (pink zone) (Alvarez et al., 1980; Kyte et al., 1985). All measured concentrations are well below those found during extraterrestrial impact events. (For interpretation of the references to color in this figure legend, the reader is referred to the web version of this article.)

observed malformed pollen and spores documented during the event (Hochuli et al., 2010; Hochuli et al., 2017). Further study of the chemical signature of coal-bearing rocks associated with the Siberian Traps sill complex may help trace the various sources of hydrocarbons in the region responsible for the event. Such a large input of carbon dioxide from combustion of coal and associated hydrocarbons into the atmosphere could be expected to have led to significant global warming, desertification, and an atmosphere rich in carbon dioxide (Sun et al., 2012).

The observed negative shift in carbon isotope ratios ($\delta^{13}C$) matches the expected increase in ^{12}C in the atmosphere from the combustion of ^{12}C-enriched coal reserves over an estimated 69 kyr duration (Shen et al., 2011). In Utah, the $\delta^{13}C$ values continue to decrease beyond the initial lithologic boundary layer, suggesting continued input of ^{12}C-enriched carbon from organic sources beyond both the initial acidification event and widespread anoxia that followed. This latter part of the $\delta^{13}C$ excursion could also be attributed to the consequences of global warming produced by the coal emissions, such as methane hydrate upwelling, and an overall decrease in photosynthesizing organisms. Together, these subsequent events likely enriched the sedimentary carbonate further in ^{12}C (Wignall, 2007).

As theorized, a scenario of a rapidly warming ocean (Song et al., 2014), which quickly became acidic, resulted in the dissolution of carbonate-rich shelled organisms (Garbelli et al., 2016). These acidic ocean waters also caused the death of many oxygen-producing photosynthesizing calcareous algae, which accumulated as dead organic matter on the ocean's floor (Wang et al., 1994; Hall-Spencer et al., 2008; Chen et al., 2011). This massive input of organic matter into the ocean floor was consumed by oxic bacteria, which used available dissolved oxygen, converting it to carbon dioxide. Oxygen-levels were further decreased in the ocean as ocean temperatures rose, since warmer ocean water holds less dissolved oxygen (Sun et al., 2012).

An initial massive combustion of coal would have enriched the atmosphere in SO_2, which interacts with water vapor and nitric oxide to form toxic sulfuric acid that could have killed terrestrial plants and animals (Wang et al., 2016). Large amounts of sulfur would have entered the anoxic marine waters as sulfate ions (SO_4^{2-}). Lacking available oxygen, these sulfate ions would have been utilized by sulfate-reducing bacteria that require high levels of organic content in the sediment and anoxic conditions (Berner, 1984). However, TOC% values across the Permian-Triassic boundary remain relatively low during the deposition of the pyrite horizons (Fig. 4; Fig. 5; Fig. 6), indicating that the sulfate-reducing bacteria utilized a different source of hydrocarbons than organic matter in the form of dead or decaying biomass, as discussed below.

Elevated Ba spikes are observed in the Utah Permian-Triassic boundary section coinciding with sulfur-enriched pyrite horizons (Fig. 14). Enriched Ba-levels have been observed in shallow marine sediment cores across the Paleocene-Eocene Thermal Maximum event (Dickens et al., 2003), where high Ba-levels have been interpreted as indicative of the sudden release of seafloor gas hydrates (Dickens et al., 2003). High-Ba zones in shallow marine sediments are indicative of the release of these seafloor gas hydrates due to the interaction of Ba^+ with sulfate. Ba^+ enters ocean water from deep seafloor hydrothermal vents. In normal oxygen-rich ocean conditions, high concentrations of SO_4^{2-} are typically confined to the ocean floor as it is produced by bioturbation by benthic organisms and oxidation of microbial H_2S (Canfield and Farquhar, 2009). At depth, SO_4^{2-} reacts with Ba^+ forming precipitates of solid barite crystals ($BaSO_4$), which accumulate in deep ocean floor sediments (Torres et al., 1996). Over time, deep ocean floor environments are enriched in Ba, but also methane molecules that are locked in a solid form within a lattice of water molecules called clathrates. As deep ocean water temperatures rise, these clathrates can sublimate into a gas, releasing large quantities of methane (CH_4) and Ba from the ocean floor. When there is a major out-gassing of methane hydrate, Ba-levels will increase in shallow nearshore marine sediments (Torres et al., 1996). Sulfate-reducing bacteria utilized the enriched ocean water concentration of methane and sulfate near the

ocean surface through microbially mediated anaerobic methane oxidation:

$$CH_4 + SO_4^{2-} \rightarrow HCO_3^- + HS^- + H_2O$$

$$HS^- + H^+ \rightarrow H_2S$$

The isotopic fractionation of sulfur isotopes resulting from these reactions explains the isotope excursions of $\delta^{34}S_{CAS}$ observed from other Permian-Triassic sections (Shen et al., 2011; Kajiwara et al., 1994; Zhang et al., 2017; Algeo et al., 2008), which show anomalies above the Permian-Triassic boundary associated with pyrite-rich (anoxic) zones. As a consequence, the oceans emitted large quantities of toxic H_2S gas, as well as methane that likely entered the atmosphere during this second stage of the Permian-Triassic mass extinction event (Song et al., 2014). In Utah, within 23,000 years of acidic conditions, shallow marine waters were anoxic and enriched in enough dissolved H_2S gas (euxinic) to begin to precipitate pyrite crystals in near shore tidal anoxic environments (Rickard, 1997; Peiffer et al., 2015). Such a scenario may account for the two closely-spaced extinction levels documented in the shallow marine Permian-Triassic section in China (Xie et al., 2005; Peiffer et al., 2015).

Coupled with the effects of global warming and acid rains, high levels of H_2S gas from the ocean has been theorized to have resulted in toxic atmospheric conditions for many terrestrial organisms (Kump et al., 2005; Meyer et al., 2008). In Utah, these anoxic nearshore ocean waters were cyclic or periodic. Quickly moving organisms, such as fish, may have been able to navigate away from these oxygen-depleted waters and were better adapted to find refuge than sessile and planktonic organisms with a fixed habitat range. This may explain the dramatic rise in fish diversity and other active swimming animals following the mass extinction event (Sun et al., 2012; Schaeffer, 1973; Dineen et al., 2014; Romano et al., 2016), with near-extinction of sessile organisms like crinoids, brachiopods, rugosa and tabulate corals, and organisms with planktonic larva (Raup, 1979; Valentine, 1986; Erwin, 1994; Benton and Twitchett, 2003; Chen et al., 2010; Chen et al., 2015; Payne and Clapham, 2012).

No evidence was found in the Utah section to suggest an extraterrestrial impact event or massive volcanism was responsible for the Permian-Triassic extinction; rather, the assembled geochemical evidence suggests a massive combustion of coal as the event responsible for Earth's largest mass extinction event. The combustion of large amounts of coal resulted in acidic ocean water, global warming, and the release of methane hydrates from the seafloor. Together these events led to a planet inhospitable to life. This study opens many avenues of inquiry, such as how much coal (and other associated hydrocarbons) was burned at the Permian-Triassic boundary during the Siberian Traps volcanism? How does this quantity compare to modern levels of hydrocarbon combustion? How close are we to a similar mass extinction happening again?

Acknowledgements

The author gratefully thanks S. Lyman for productive discussion of Hg detection and E. Swanner for productive discussion of pyrite formation. A. Lonero and D. Newell for help running samples through the ICP-MS and Mass-Spec. at Utah State University in Logan, and L. Jolley, Z. Jolley-Burger, and F. Jolley-Burger for help collecting samples in the field. Personal funds were used to conducted the research.

References

Algeo, T., Shen, Y., Zhang, T., Lyons, T., Bates, S., Rowe, H., Nguyen, T.K.T., 2008. Association of ^{34}S-depleted pyrite layers with negative carbonate δ^{13}C excursions at the Permian-Triassic boundary: evidence for upwelling of sulfidic deep-ocean water masses. Geochem. Geophys. Geosyst. 9 (Q04025), 1–10. https://doi.org/10.1029/2007gc001823.

Alvarez, W., O'Connor, D., 2002. Permian-Triassic boundary in the southwestern United States: hiatus or continuity. In: Koeberl, C., MacLeod, K.G. (Eds.), Catastrophic Events and Mass Extinctions: Impacts and Beyond. vol. 356. pp. 385–393. https://doi.org/10.1130/0-8137-2356-6.385. (GSA special Paper).

Alvarez, L.W., Alvarez, W., Asaro, F., Michel, H.V., 1980. Extraterrestrial cause for the Cretaceous-Tertiary extinction. Science 208, 1095–1108. https://doi.org/10.1126/science.208.4448.1095.

Arnold, J., Gustin, M.S., Weisberg, P., 2017. Evidence for nonstomatal uptake of Hg by and translocation of Hg from foliage to tree ring in Austrian pine. Environ. Sci. Technol. 3, 1174–1182. https://doi.org/10.1021/acs.est.7b04468.

Baresel, B., Bucher, H., Bagherpour, B., Brosse, M., Guodun, K., Schaltegger, U., 2017. Timing of global regression and microbial bloom linked with the Permian-Triassic boundary mass extinction: implications for driving mechanisms. Sci. Rep. 7 (43630), 1–8. https://doi.org/10.1038/srep43630.

Baud, A., Magaritz, M., Holser, W.T., 1989. Permian-Triassic of the Tethys: carbon isotope studies. Geol. Rundsch. 78/2, 649–677. https://doi.org/10.1007/bf01776196.

Beerling, D.J., Harfoot, M., Lomax, B., Pyle, J.A., 2007. The stability of the stratospheric ozone layer during the end-Permian eruption of the Siberian. Traps. Phil. Trans. R. Soc. A 365, 1843–1866. https://doi.org/10.1098/rsta.2007.2046.

Benton, M.J., Twitchett, R.J., 2003. How to kill (almost) all life: the end-Permian extinction event. Trends Ecol. Evol. 18, 358–365. https://doi.org/10.1016/s0169-5347(03)00093-4.

Berner, R.A., 1984. Sedimentary pyrite formation: an update. Geochim. Cosmochim. Acta 48, 605–615. https://doi.org/10.1016/0016-7037(84)90089-9.

Berner, R.A., 2002. Examination of hypotheses for the Permo-Triassic boundary extinction by carbon cycle modeling. Proc. Natl. Acad. Sci. U. S. A. 99, 4172–4177. https://doi.org/10.1073/pnas.032095199.

Berner, R.A., 2006. Carbon, sulfur, and O_2 across the Permian-Triassic boundary. J. Geochem. Explor. 88, 416–418. https://doi.org/10.1016/j.gexplo.2005.08.088.

Black, B.A., Elkins-Tanton, L.T., Rowe, M.C., Peate, I.U., 2012. Magnitude and consequences of volatile release from Siberian Traps. Earth Planet. Sci. Lett. 317-318, 363–373. https://doi.org/10.1016/j.epsl.2011.12.001.

Block, C., Dams, R., 1975. Lead contents of coal, coal ash and fly ash. Water Air Soil Pollut. 5, 207–211. https://doi.org/10.1007/bf00282962.

Bond, D.P.G., Wignall, P.B., 2010. Pyrite framboid study of marine Permian-Triassic boundary sections: a complex anoxic event and its relationship to contemporaneous mass extinction. Geol. Soc. Am. Bull. 122, 1265–1279. https://doi.org/10.1130/b30042.1.

Brayard, A., Krumenacker, L.J., Botting, J.P., Jenks, J.F., Bylund, K.G., Fara, E., Vennin, E., Olivier, N., Goudemand, N., Saucède, T., Charbonnier, S., Romano, C., Doguzhaeva, L., Thuy, B., Hautmann, M., Stephen, D.A., Thomazo, C., Escarguel, G., 2017. Unexpected early Triassic marine ecosystem and the rise of the modern evolutionary fauna. Sci. Adv. 3, e1602159. https://doi.org/10.1126/sciadv.1602159.

Brennecka, G.A., Herrmann, A.D., Algeo, T.J., Anbar, A.D., 2011. Rapid expansion of oceanic anoxia immediately before the end-Permian mass extinction. Proc. Natl. Acad. Sci. U. S. A. 108, 17631–17634. https://doi.org/10.1073/pnas.1106039108.

Briggs, P.H., 1997. "Determination of 25 elements in coal ash from 8 Argonne premium coal samples by Inductively Coupled Argon Plasma-Atomic Emission Spectrometry" in The chemical analysis of Argonne premium coal samples, C. A. Palmer ed. U.S. Geol. Surv. Bull. 2144, 39–44. https://pubs.usgs.gov/bul/2144/report.pdf.

Brookfield, M.E., Shellnutt, J.G., Qi, L., Hannigan, R., Bhat, G.M., Wignall, P.B., 2010. Platinum element group variations at the Permo-Triassic boundary in Kashmir and British Columbia and their significance. Chem. Geol. 272, 12–19. https://doi.org/10.1016/j.chemgeo.2010.01.008.

Burgess, S.D., Bowring, S., Shen, S.-Z., 2014. High-precision timeline for Earth's most severe extinction. Proc. Natl. Acad. Sci. U. S. A. 111, 3316–3321. https://doi.org/10.1073/pnas.1317692111.

Burgess, S.D., Murihead, J.D., Bowring, S.A., 2017. Initial pulse of Siberian Traps sills as the trigger of the end-Permian mass extinction. Nat. Commun. 8 (164), 1–6. https://doi.org/10.1038/s41467-017-00083-9.

Canfield, D.E., Farquhar, J., 2009. Animal evolution, bioturbation, and the sulfate concentration of the oceans. Proc. Natl. Acad. Sci. U. S. A. 106, 8123–8127. https://doi.org/10.1073/pnas.0902037106.

Chen, Z.-Q., Tong, J., Liao, Z.-T., Chen, J., 2010. Structural changes of marine communities over the Permian-Triassic transition: ecologically assessing the end-Permian mass extinction and its aftermath. Global Plan. Change 73, 123–140. https://doi.org/10.1016/j.gloplacha.2010.03.011.

Chen, L., Wang, Y., Xie, S., Kershaw, S., Dong, M., Yang, H., Liu, H., Algeo, T.J., 2011. Molecular records of microbialites following the end-Permian mass extinction in Chongyang, Hubei Province, South China. Palaeogeogr. Palaeoclimatol. Palaeoecol. 308, 151–159. https://doi.org/10.1016/j.palaeo.2010.09.010.

Chen, J., Tong, J., Song, H., Luo, M., Huang, Y., Xiang, Y., 2015. Recovery pattern of brachiopods after the Permian-Triassic crisis in South China. Palaeogeogr. Paleoclimatol. Palaeoecol. 433, 91–105. https://doi.org/10.1016/j.palaeo.2015.05.020.

Dickens, G.R., Fewless, T., Thomas, E., Bralower, T.J., 2003. Excess barite accumulations during the Paleocene-Eocene thermal Maximum: massive input of dissolved barium from seafloor gas hydrate reservoirs. In: Wing, S.L., Gingerich, P.D., Schmitz, B., Thomas, E. (Eds.), Causes and Consequences of Globally Warm Climates in the early Paleogene. 369. pp. 11–23. https://doi.org/10.1130/0-8137-2369-8.11. (GSA special Paper 2003).

Dineen, A.A., Fraiser, M.L., Sheehan, P.M., 2014. Quantifying functional diversity in pre- and post-extinction paleocommunities: a test of ecological restructuring after the end-Permian mass extinction. Earth-Sci. Rev. 136, 339–349. https://doi.org/10.1016/j.earscirev.2014.06.002.

Doughten, M.W., 1997. "Determination of select elements in coal ash from eight Argonne premium coal samples by atomic absorption spectrometry and atomic emission

spectrometry" in the chemical analysis of Argonne premium coal samples, C. A. Palmer ed. *U.S.* Geol. Den. Surv. Bull. 2144, 33–37. https://pubs.usgs.gov/bul/2144/report.pdf.

Erwin, D.H., 1994. The Permo-Triassic extinction. Nature 367, 231–236. https://doi.org/10.1038/367231a0.

Fraiser, M.L., Bottjer, D.J., 2007. Elevated atmospheric CO_2 and the delayed biotic recovery from the end-Permian mass extinction. Palaeogeogr. Palaeoclimatol. Palaeoecol. 252, 164–175. https://doi.org/10.1016/j.palaeo.2006.11.041.

Garbelli, C., Angiolini, L., Shen, S.-Z., 2016. Biomineralization and global change: a new perspective for understanding the end-Permian extinction. Geology 45, 19–22. https://doi.org/10.1130/g38430.1.

Grasby, S.E., Sanei, H., Beauchamp, B., 2011. Catastrophic dispersion of coal fly-ash into oceans during the latest Permian extinction. Nat. Geosci. 4, 104–107. https://doi.org/10.1038/ngeo1069.

Grasby, S.E., Beauchamp, B., Bond, D.P.G., Wignall, P.B., Sanei, H., 2016. Mercury anomalies associated with three extinction events (Capitanian Crisis, latest Permian extinction and the Smithian/Spathian extinction) in NW Pangea. Geol. Mag. 153, 285–297. https://doi.org/10.1017/s0016756815000436.

Grasby, S.E., Shen, W., Yin, R., Gleason, J.D., Blum, J.D., Lepak, R.F., Hurley, J.P., Beauchamp, B., 2017. Isotopic signatures of mercury contamination in latest Permian oceans. Geology 45, 55–58. https://doi.org/10.1130/G38487.1.

Grice, K., Cao, C., Love, G.D., Böttcher, M.E., Twitchett, R.J., Grosjean, E., Summons, R.E., Turgeon, S.C., Summons, R.E., Turgeon, S.C., Dunning, W., Jin, Y., 2005. Photic zone euxinia during the Permian-Triassic superanoxic event. Science 307, 706–709. https://doi.org/10.1126/science.1104323.

Gustin, M.S., Lindberg, S.E., Weisberg, P.J., 2008. An update on the natural sources and sinks of atmospheric mercury. Appl. Geochem. 23, 482–493. https://doi.org/10.1016/j.apgeochem.2007.12.010.

Hall-Spencer, J.M., Rodolfo-Metalpa, R., Martin, S., Ransome, E., Fine, M., Turner, S.M., Rowley, S.J., Tedesco, D., Buia, M.-C., 2008. Volcanic carbon dioxide vents show ecosystem effects of ocean acidification. Nature 454, 96–99. https://doi.org/10.1038/nature07051.

Hays, J.D., Imbrie, J., Shackleton, N.J., 1976. Variations in the Earth's Orbit: Pacemaker of the Ice Ages. Science 194, 1121–1132. https://doi.org/10.1126/science.194.4270.1121.

Heckert, A.B., Chure, D.J., Voris, J.T., Harrison, A.A., Thomson, T.J., 2015. Stratigraphy, correlation, and age of the Moenkopi Formation in the vicinity of Dinosaur National Monument, eastern Uinta Basin, Utah and Colorado, USA. In: Vanden Berg, M.D., Ressetar, R., Birgenheier, L.P. (Eds.), Geology of Utah's Uinta Basin and Uinta Mountains. 44. Utah Geological Association Publication, pp. 1–12.

Henderson, C.M., 2018. Permian conodont biostratigraphy, *in* Lucas, S.G. And Shen, S.Z. (eds) the Permian Timescale. Geol. Soc. Lond., Spec. Publ. 450, 119–142.

Hochuli, P.A., Hermann, E., Vigran, J.O., Bucher, H., Weissert, H., 2010. Rapid demise and recovery of plant ecosystems across the end-Permian extinction event. Global Plan. Change 74, 144–155. https://doi.org/10.1016/j.gloplacha.2010.10.004.

Hochuli, P.A., Schneebeli-Hermann, E., Mangerud, G., Bucher, H., 2017. Evidence for atmospheric pollution across the Permian-Triassic transition. Geology 45, 1123–1126. https://doi.org/10.1130/g39496.1.

Hofmann, R., Hautmann, M., Bucher, H., 2013. New paleoecological look at the Dinwoody Formation (lower Triassic, Western USA): Intrinsic versus extrinsic controls on ecosystem recovery after the end-Permian mass extinction. J. Paleontol. 87, 854–880. https://doi.org/10.1666/12-153.

Huang, T., Chen, Z.-Q., Algeo, T.J., Zhao, L., Baud, A., Bhat, G.M., Zhang, L., Guo, Z., 2019. Two-stage marine anoxia and biotic response during the Permian-Triassic transition in Kashmir, northern India: pyrite framboid evidence. Glob. Planet. Chang. 172, 124–139. https://doi.org/10.1016/j.gloplacha.2018.10.002.

Isozaki, Y., 1997. Permo-Triassic boundary super anoxia and stratified super ocean: records from lost deep sea. Science 276, 235–238. https://doi.org/10.1126/science.276.5310.235.

Iyaka, Y.A., 2011. Nickel in soils: a review of its distribution and impacts. Sci. Res. Essays 6, 6774–6777. https://doi.org/10.5897/srex11.035.

Jin, Y.G., Wang, Y., Wang, W., Shang, Q.H., Cao, C.Q., Erwin, D.H., 2000. Pattern of marine mass extinction near the Permian-Triassic boundary in South China. Science 289, 432–436. https://doi.org/10.1126/science.289.5478.432.

Kaiho, K., Kajiwara, Y., Nakano, T., Miura, Y., Kawahata, H., Tazaki, K., Ueshima, M., Chen, Z., Shi, G.R., 2001. End-Permian catastrophe by a bolide impact: evidence of a gigantic release of sulfur from the mantle. Geology 29, 815–818. https://doi.org/10.1130/0091-7613(2001)029<0815:epcbab>2.0.co;2.

Kajiwara, Y., Yamakita, S., Ishida, K., Ishiga, H., Imai, A., 1994. Development of a largely anoxic stratified ocean and its temporary massive mixing at the Permian/Triassic boundary supported by the sulfur isotope record. Palaeogeogr. Palaeoclimatol. Palaeoecol. 111, 367–379. https://doi.org/10.1016/0031-0182(94)90072-8.

Kakuwa, Y., 1996. Permian-Triassic mass extinction event recorded in bedded chert sequence in southwestern Japan. Palaeogeogr. Palaeoclimatol. Palaeoecol. 121, 35–51. https://doi.org/10.1016/0031-0182(95)00070-4.

Kakuwa, Y., 2008. Evaluation of palaeo-oxygenation of the ocean bottom across the Permian-Triassic boundary. Global Plan. Change 63, 40–56. https://doi.org/10.1016/j.gloplacha.2008.05.002.

Kershaw, S., Zhang, T., Lan, G., 1999. A ?microbialite carbonate crust at the Permian-Triassic boundary in South China, and its palaeoenvironmental significance. Palaeogeogr. Palaeoclimatol. Palaeoecol. 146, 1–18. https://doi.org/10.1016/s0031-0182(98)00139-4.

Kershaw, S., Tang, H., Li, Y., Guo, L., 2018. Oxygenation in carbonate microbialites and associated facies after the end-Permian mass extinction: problems and potential solutions. J. Palaeogeogr. 2018. https://doi.org/10.1016/j.jop.2017.10.001.

Korte, C., Kozur, H.W., 2010. Carbon-isotope stratigraphy across the Permian-Triassic boundary: a review. J. Asian Earth Sci. 39, 215–235. https://doi.org/10.1016/j.jseaes.2010.01.005.

Korte, C., Kozur, H.W., Joachimski, M.M., Strauss, H., Veizer, J., Schwark, L., 2004. Carbon, sulfur, oxygen and strontium isotope records, organic geochemistry and biostratigraphy across the Permian/Triassic boundary in Abadeh, Iran. Int. J. Earth Sci. 93, 565–581. https://doi.org/10.1007/s00531-004-0406-7.

Krull, E.S., Retallack, G.J., Campbell, H.J., Lyon, G.L., 2000. $\delta^{13}C_{org}$ chemostratigraphy of the Permian-Triassic boundary in the Maitai Group, New Zealand: Evidence for high-latitudinal methane release. New Zealand J. Geol. Geophys. 43, 21–32. https://doi.org/10.1080/00288306.2000.9514868.

Krull, E.A., Lehrmann, D.J., Druke, D., Kessel, B., Yi, Y., Li, R., 2004. Stable carbon isotope stratigraphy across the Permian-Triassic boundary in shallow marine carbonate platforms, Nanpanjiang Basin, South China. Palaeogeogr. Palaeoclimatol. Palaeoecol. 204, 297–315. https://doi.org/10.1016/s0031-0182(03)00732-6.

Kummel, B., 1954. Triassic stratigraphy of southeastern Idaho and adjacent areas. Geol. Surv. Prof. Pap. 254-H, 165–194.

Kump, L., Pavlov, A., Arthur, M.A., 2005. Massive release of hydrogen sulfide to the surface ocean and atmosphere during intervals of oceanic anoxia. Geology 33, 397–400. https://doi.org/10.1130/g21295.1.

Kyte, F.T., Smit, J., Wasson, J.T., 1985. Siderophile interelement variations in the Cretaceous-Tertiary boundary sediments from Caravaca, Span. Earth Planet. Sci. Lett. 73, 183–195. https://doi.org/10.1016/0012-821x(85)90067-6.

Latyshev, A.V., Veselovshiy, R.V., Ivanov, A.V., 2018. Paleomagnetism of the Permian-Triassic intrusions from the Tunguska syncline and the Angara-Taseeva depression, Siberian Traps large igneous province: evidence of contrasting styles of magmatism. Tectonophysics 723, 41–55. https://doi.org/10.1016/j.tecto.2017.11.035.

Le Vaillant, M., Barnes, S.J., Mungall, J.E., Mungall, E.L., 2017. Role of degassing of the Noril'sk nickel deposits in the Permian-Triassic mass extinction event. Proc. Natl. Acad. Sci. U. S. A. 114, 2485–2490. https://doi.org/10.1073/pnas.1611086114.

Leavitt, S.W., 1982. Annual volcanic carbon dioxide emission: an estimate from eruption chronologies. *Environ.* Geology 4, 15–21. https://doi.org/10.1007/bf02380495.

Lehrmann, D.J., Payne, J.L., Felix, S.V., Dillett, P.M., 2003. Permian-Triassic boundary sections from shallow-marine carbonate platforms of the Nanpanjiang Basin, South China: implications for oceanic conditions associated with the end-Permian extinction and its aftermath. Palaios 18, 138–152. https://doi.org/10.1669/0883-1351(2003)18<138:pbsfsc>2.0.co;2.

Liao, W., Bond, D.P.G., Wang, Y., He, L., Yang, H., Weng, Z., Li, G., 2017. An extensive anoxic event in the Triassic of the South China block: a pyrite framboid study from Dajiang and its implications for the cause(s) of oxygen depletion. Palaeogeogr. Palaeoclimatol. Palaeoecol. 486, 86–95. https://doi.org/10.1016/j.palaeo.2016.11.012.

Liu, S.-A., Wu, H., Shen, S.-Z., Jiang, G., Zhang, S., Lv, Y., Zhang, H., Li, S., 2017. Zinc isotope evidence for intensive magmatism immediately before the end-Permian mass extinction. Geology 45, 343–346. https://doi.org/10.1130/g38644.1.

Luo, G., Kump, L.R., Wang, Y., Tong, J., Arthur, M.A., Yang, H., Huang, J., Yin, H., Xie, S., 2010. Isotopic evidence for an anomalously low oceanic sulfate concentration following the end-Permian mass extinction. Earth Planet. Sci. Lett. 300, 101–111. https://doi.org/10.1016/j.epsl.2010.09.041.

Magaritz, M., Bär, R., Baud, A., Holser, W.T., 1988. The carbon-isotope shift at the Permian/Triassic boundary in the southern Alps is gradual. Nature 331, 337–339. https://doi.org/10.1038/331337a0.

Meyer, K.M., Kump, L.R., Ridgwell, A., 2008. Biogeochemical controls on photic-zone euxinia during the end-Permian mass extinction. Geology 36, 747–750. https://doi.org/10.1130/g24618a.1.

Meyer, K.M., Yu, M., Jost, A.B., Kelly, B.M., Payne, J.L., 2011. $\delta^{13}C$ evidence that high primary productivity delayed recovery from end-Permian mass extinction. Earth Planet. Sci. Lett. 302, 378–384. https://doi.org/10.1016/j.epsl.2010.12.033.

Meyer, K.M., Yu, M., Lehrmann, D., Van de Schootbrugge, B., Payne, J.L., 2013. Constraints on early Triassic carbon cycle dynamics from paired organic and inorganic carbon isotope records. Earth Planet. Sci. Lett. 361, 429–435. https://doi.org/10.1016/j.epsl.2012.10.035.

Miller, A.K., Cline, L.M., 1934. The Cephalopods of the Phosphoria Formation of Northwestern United States. J. Paleontol. 8, 281–302.

Müller, G., Gastner, M., 1971. The "karbonat-bomb", a simple device for the determination of the carbonate content in sediments, soils and other materials. Neues Jahrb. Min. Abh. 10, 466–469.

Mundil, R., Ludwig, K.R., Metcalfe, I., Renne, P.R., 2004. Age and timing of the Permian mass extinctions: U/Pb dating of closed-system zircons. Science 305, 1760–1763. https://doi.org/10.1126/science.1101012.

Natusch, D.F.S., Wallace, J.R., Evans Jr., C.A., 1974. Toxic trace elements: preferential concentrations in respirable particles. Science 183, 202–204. https://doi.org/10.1126/science.183.4121.202.

Newell, N.D., Kummel, B., 1942. Lower Eo-Triassic stratigraphy, western Wyoming and southeastern Idaho. Bull. Geol. Soc. Am. 53, 937–996. https://doi.org/10.1130/gsab-53-937.

Ochoa-González, R., Weiss, D., 2015. Zinc isotope variability in three coal-fired power plants: a predictive model for determining isotopic fractionation during combustion. Environ. Sci. Technol. 49, 12560–12567. https://doi.org/10.1021/acs.est.5b02402.

Ogden, D.E., Sleep, N.H., 2012. Explosive eruption of coal and basalt and the end-Permian mass extinction. Proc. Natl. Acad. Sci. U. S. A. 109 (1), 59–62. https://doi.org/10.1073/pnas.1118675109.

Paull, R.K., 1988. Distribution pattern of lower Triassic (Scythian) conodonts in the Western United States: Documentation of the Pakistan connection. Palaios 3, 598–605. https://doi.org/10.2307/3514448.

Paull, R.K., Paull, R.A., 1982. Permian-Triassic unconformity in the Terrace Mountains, northwestern Utah. Geology 10, 582–587. https://doi.org/10.1130/0091-

7613(1982)10<582:puittm>2.0.co;2.
Paull, R.K., Paull, R.A., 1994. Shallow marine sedimentary facies in the earliest Triassic (Griesbachian) Cordilleran miogeocline, U.S. Sediment. Geol. 93, 181–191. https://doi.org/10.1016/0037-0738(94)90004-3.
Payne, J.L., Clapham, M.E., 2012. End-Permian mass extinction in the oceans: an ancient analog for the twenty-first century? Annu. Rev. Earth Planet. Sci. 40, 89–111. https://doi.org/10.1146/annurev-earth-042711-105329.
Payne, J.L., Lehrmann, D.J., Wei, J., Orchard, M.J., Schrag, D.P., Knoll, A.H., 2004. Large perturbations of the carbon cycle during recovery from the end-Permian extinction. Science 305, 506–509. https://doi.org/10.1126/science.1097023.
Payne, J.L., Lehrmann, D.J., Follett, D., Seibel, M., Kump, L.R., Riccardi, A., Altiner, D., Sano, H., Wei, J., 2007. Erosional truncation of uppermost Permian shallow-marine carbonates and implications for Permian-Triassic boundary events. Geol. Soc. Am. Bull. 119, 771–784. https://doi.org/10.1130/b26091.1.
Peiffer, S., Behrends, T., Hellige, K., Larese-Casanova, P., Wan, M., Pollok, K., 2015. Pyrite formation and mineral transformation pathways upon sulfidation of ferric hydroxides depend on mineral type and sulfide concentrations. Chem. Geol. 400, 44–55. https://doi.org/10.1016/j.chemgeo.2015.01.023.
Rampino, M.R., Prokoph, A., Adler, A., 2000. Tempo of the end-Permian event: high-resolution cyclostratigraphy at the Permian-Triassic boundary. Geology 28, 643–646. https://doi.org/10.1130/0091-7613(2000)028<0643:totepe>2.3.co;2.
Rampino, M.R., Rodriguez, S., Baransky, E., Cai, Y., 2017. Global nickel anomaly links Siberian Traps eruptions and the latest Permian mass extinction. Sci. Rep. 7, 12416. https://doi.org/10.1038/s41598-017-12759-9.
Raup, D.M., 1979. Size of the Permo-Triassic bottleneck and its evolutionary implications. Science 206, 217–218. https://doi.org/10.1126/science.206.4415.217.
Reichow, M.K., Pringle, M.S., Al'Mukhamedov, A.I., Allen, M.B., Andreichev, V.L., Buslov, M.M., Davies, C.E., Fedoseev, G.S., Fitton, J.G., Inger, S., Medvedev, A.Y., Mitchell, C., Punchkov, V.N., Safonova, L.Y., Scott, R.A., Saunders, A.D., 2009. The timing and extent of the eruption of the Siberian Traps large igneous provinces: implications for the end-Permian environmental crisis. Earth Planet. Sci. Lett. 277, 9–20. https://doi.org/10.1016/j.epsl.2008.09.030.
Renne, P.R., Basu, A.R., 1991. Rapid eruption of the Siberian Traps flood basalts at the Permo-Triassic boundary. Science 253, 176–179. https://doi.org/10.1126/science.253.5016.176.
Renne, P.R., Zichao, Z., Richards, M.A., Black, M.T., Basu, A.R., 1995. Synchrony and causal relations between Permian-Triassic boundary crises and Siberian flood volcanism. Science 269, 1413–1416. https://doi.org/10.1126/science.269.5229.1413.
Riccardi, A., Kump, L.R., Arthur, M.A., D'Hondt, S., 2007. Carbon isotopic evidence for chemocline upward excursions during the end-Permian event. Palaeogeogr. Palaeoclimatol. Palaeoecol. 248, 73–81. https://doi.org/10.1016/j.palaeo.2006.11.010.
Rickard, D., 1997. Kinetics of pyrite formation by the H_2S oxidation of iron (II) monosulfide in aqueous solutions between 25 and 125°C: the rate equation. Geochim. Cosmochim. Acta 61, 115–134. https://doi.org/10.1016/s0016-7037(96)00321-3.
Romano, C., Koot, M.B., Kogan, I., Brayard, A., Minikh, A.V., Brinkmann, W., Bucher, H., Kriwet, J., 2016. Permian-Triassic Osteichthyes (bony fishes) diversity dynamics and body size evolution. Biol. Rev. 91, 106–147. https://doi.org/10.1111/brv.12161.
Sanei, H., Grasby, S.E., Beauchamp, B., 2012. Latest Permian mercury anomalies. Geology 40, 63–66. https://doi.org/10.1130/g32596.1.
Schaeffer, B., 1973. "Fishes and the Permian-Triassic boundary" in the Permian and Triassic systems and their mutual boundary. Mem. Canadian Soc. Petro. Geol. 2, 487–493.
Schoepfer, S.D., Henderson, C.M., Garrison, G.H., Ward, P.D., 2012. Cessation of a productive coastal upwelling system in the Pathalassic Permian-Triassic boundary. Palaeogeogr. Palaeoclimatol. Palaeoecol. 313-314, 181–188. https://doi.org/10.1016/j.palaeo.2011.10.019.
Schoepfer, S.D., Henderson, C.M., Garrison, G.H., Foriel, J., Ward, P.D., Selby, D., Hower, J.C., Algeo, T.J., Shen, Y., 2013. Termination of a continent-margin upwelling system at the Permian-Triassic boundary (Opal Creek, Alberta, Canada). Glob. Planet. Chang. 105, 21–35. https://doi.org/10.1016/j.gloplacha.2012.07.005.
Schubert, J.K., Bottjer, D.J., 1995. Aftermath of the Permian-Triassic mass extinction event: Paleoecology of lower Triassic carbonates in the western USA. Palaeogeogr. Palaeoclimatol. Palaeoecol. 116, 1–39. https://doi.org/10.1016/0031-0182(94)00093-n.
Sheldon, N.D., 2006. Abrupt chemical weathering increase across the Permian-Triassic boundary. Palaeogeogr. Palaeoclimatol. Palaeoecol. 231, 315–321. https://doi.org/10.1016/j.palaeo.2005.09.001.
Shen, W., Lin, Y., Xu, L., Li, J., Wu, Y., Sun, Y., 2007. Pyrite framboids in the Permian-Triassic boundary section at Meishan, China: evidence for dysoxic deposition. Palaeogeogr. Palaeoclimatol. Palaeoecol. 253, 323–331. https://doi.org/10.1016/j.palaeo.2007.06.005.
Shen, S.-Z., Crowley, J.L., Wang, Y., Bowring, S.A., Erwin, D.H., PSadler, P.M., Cao, C.-Q., Rothman, D.H., Henderson, C.M., Ramezani, J., Zhang, H., Shen, Y., Wang, X.-D., Wang, W., Mu, L., Li, W.-Z., Tang, Y.-G., Liu, X.-L., Liu, L.-J., Zeng, Y., Jin, Y.-G., 2011. Calibrating the end-Permian mass extinction. Science 334, 1367–1372. https://doi.org/10.1126/science.1213454.
Shen, S.-Z., Ramezani, J., Chen, J., Cao, C.-Q., Erwin, D.H., Zhang, H., Xiang, L., Schoepfer, S.D., Henderson, C.M., Zheng, Q.-F., Bowring, S.A., Wang, Y., Li, X.-H., Yuan, D.-X., Zhang, Y.-C., Mu, L., Wang, J., Wu, Y.-S., 2018. A sudden end-Permian mass extinction in South China. Geol. Soc. Am. Bull. https://doi.org/10.1130/B31909.1.
Smichowski, P., Gómez, D., Rosa, S., Polla, G., 2003. Trace elements content in size-classified volcanic ashes as determined by inductively coupled plasma-mass spectrometry. Microchem. J. 75, 109–117. https://doi.org/10.1016/s0026-265x(03)00089-4.
Smith, H.P., 1969. The Thaynes Formation of the Moenkopi Group North-Central Utah. Unpublished Dissertation University of Utah, Salt Lake City, pp. 1–169.
Song, H., Tong, J., Chen, Z.Q., 2009. Two episodes of foraminiferal extinction near the Permian-Triassic boundary at the Meishan section, South China. Aust. J. Earth Sci. 56, 765–773. https://doi.org/10.1080/08120090903002599.
Song, H., Wignall, P.B., Tong, J., Bond, D.P.G., Song, H., Lai, X., Zhang, K., Wang, H., Chen, Y., 2012. Geochemical evidence from bio-apatite for multiple oceanic anoxic events during Permian-Triassic transition and the link with end-Permian extinction and recovery. Earth Planet. Sci. Lett. 353-354, 12–21. https://doi.org/10.1016/j.epsl.2012.07.005.
Song, H., Tong, J., Algeo, T.J., Horacek, M., Qiu, H., Song, H., Tian, L., Chen, Z.-Q., 2013. Large vertical $\delta^{13}C_{DIC}$ gradients in early Triassic seas of the South China craton: implications for oceanographic changes related to Siberian Traps volcanism. Glob. Planet. Chang. 105, 7–20. https://doi.org/10.1016/j.gloplacha.2012.10.023.
Song, H., Wignall, P.B., Chu, D., Tong, J., Sun, Y., Song, H., He, W., Tian, L., 2014. Anoxia/high temperature double whammy during the Permian-Triassic marine crisis and its aftermath. Sci. Rep. 4 (4132), 1–7. https://doi.org/10.1038/srep04132.
Sperling, E.A., Ingle, J.C., 2006. A Permian-Triassic boundary section at Quinn River Crossing, northwestern Nevada, and implications for the cause of the Early Triassic chert gap on the western Pangean margin. Geol. Soc. Am. Bull. 118, 733–746. https://doi.org/10.1130/b25803.1.
Sprinkel, D.A., Park, B., Stevens, M., 2000. Geological road guide to Sheep Creek Canyon geological area, northeastern Utah. Utah Geol. Assoc. 29, 1–14. https://www.utahgeology.org/road_logs/uga-29_first_edition/...guide/sheepcrk.pdf.
Straub, M., Sigman, D.M., Ren, H., Martinez-Garcia, A., Meckler, A.N., Hain, M.P., Haung, G.H., 2013. Changes in North Atlantic nitrogen fixation controlled by ocean circulation. Nature 501, 200–203. https://doi.org/10.1038/nature12397.
Sun, Y., Joachimski, M.M., Wignall, P.B., Yan, C., Chen, Y., Jiang, H., Wang, L., Lai, X., 2012. Lethally hot temperatures during the early Triassic greenhouse. Science 338, 366–370. https://doi.org/10.1126/science.1224126.
Svensen, H., Planke, S., Polozov, A.G., Schmidbauer, N., Corfu, F., Podladchikov, Y.Y., Jamtveit, B., 2009. Siberian gas venting and the end-Permian environmental crisis. Earth Planet. Sci. Lett. 277, 490–500. https://doi.org/10.1016/j.epsl.2008.11.015.
Sweet, W.C., Bergström, S.M., 1986. Conodonts and Biostratigraphic correlation. Annu. Rev. Earth Planet. Sci. 14, 85–112. https://doi.org/10.1146/annurev.ea.14.050186.000505.
Szmytkiewicz, A., Zalewska, T., 2014. Sediment deposition and accumulation rates determined by sediment trap and ^{210}Pb isotope methods in the Outer Puck Bay (Baltic Sea). Oceanologia 56, 85–106. https://doi.org/10.5697/oc.56-1.085.
Taylor, H.E., Lichte, F.E., 1980. Chemical composition of Mount St. Helens volcanic ash. Geophys. Res. Lett. 7, 949–952. https://doi.org/10.1029/gl007i011p00949.
Tian, L., Tong, J., Algeo, T.J., Song, H., Chu, D., Shi, L., Bottjer, D.J., 2014. Reconstruction of early Triassic Ocean redox conditions based on framboidal pyrite from the Nanpanjiang Basin, South China. Palaeogeogr. Palaeoclimatol. Palaeoecol. 412, 68–79. https://doi.org/10.1016/j.palaeo.2014.07.018.
Torres, M.E., Brumsack, H.J., Bohrmann, G., Emeis, K.C., 1996. Barite fronts in continental margin sediments: a new look at barium remobilization in the zone of sulfate reduction and formation of heavy barites in diagenetic fronts. Chem. Geol. 127, 125–139. https://doi.org/10.1016/0009-2541(95)00090-9.
Valentine, J.W., 1986. The Permian-Triassic extinction event and invertebrate developmental modes. Bull. Mar. Sci. 39, 607–615.
Wang, K., Geldsetzer, H.H.J., Krouse, H.R., 1994. Permian-Triassic extinction: organic $\delta^{13}C$ evidence from British Columbia, Canada. Geology 22, 580–584. https://doi.org/10.1130/0091-7613(1994)022<0580:pteoce>2.3.co;2.
Wang, G., Zhang, R., Gomez, M.E., Yang, L., Zamora, M.L., Hu, M., Lin, Y., Peng, J., Guo, S., Meng, J., Li, J., Cheng, C., Hu, T., Ren, Y., Wang, Y., Gao, J., Cao, J., An, Z., Zhou, W., Li, G., Wang, J., Tian, P., Marrero-Ortiz, W., Secrest, J., Du, Z., Zheng, J., Shang, D., Zeng, L., Shao, M., Wang, W., Huang, Y., Wang, Y., Zhu, Y., Li, Y., Hu, J., Pan, B., Cai, L., Cheng, Y., Ji, Y., Zhang, F., Rosenfeld, D., Liss, P.S., Duce, R.A., Kolb, C.E., Molina, M.J., 2016. Persistent sulfate formation from London fog to Chinese haze. Proc. Natl. Acad. Sci. U. S. A. 113, 13630–13635. https://doi.org/10.1073/pnas.1616540113.
Wang, X., Cawood, P.A., Zhao, H., Grasby, S.E., Chen, Z.-Q., Wignall, P.B., Lv, Z., Han, C., Collinson, J.W., 2018. Mercury anomalies across the end Permian mass extinction in South China from shallow and deep-water depositional environments. Earth Planet. Sci. Lett. 496, 159–167. https://doi.org/10.1016/j.epsl.2018.05.044.
Wardlaw, B.R., Collinson, J.W., 1979. Biostratigraphic zonation of the Park City Group. U.S. Geol. Surv. Prof. Pap. 1163-D, 17–22.
Wardlaw, B.R., Collinson, J.W., 1986. Paleontology and deposition of the Phosphoria Formation. Contrib. Geol. 24, 107–142.
Wignall, P.B., 2007. The end-Permian mass extinction – how bad did it get? Geobiology 5, 303–309. https://doi.org/10.1111/j.1472-4669.2007.00130.x.
Wignall, P.B., Hallam, A., 1992. Anoxia as a cause of the Permian/Triassic mass extinction: facies evidence from northern Italy and the western United States. Palaeogeogr. Palaeoclimatol. Palaeoecol. 93, 21–45. https://doi.org/10.1016/0031-0182(92)90182-5.
Wignall, P.B., Twitchett, R.J., 2002. Extent, duration, and nature of the Permian-Triassic superanoxic event. In: Koeberl, C., MacLeod, K.G. (Eds.), Catastrophic Events and Mass Extinctions: Impacts and Beyond. 356. pp. 395–413. https://doi.org/10.1130/0-8137-2356-6.395. (GSA special Paper).
Wignall, P.B., Newton, R., Brookfield, M.E., 2005. Pyrite framboid evidence for oxygen-poor deposition during the Permian-Triassic crisis in Kashmir. Palaeogeogr. Palaeoclimatol. Palaeoecol. 216, 183–188. https://doi.org/10.1016/j.palaeo.2004.10.009.
Winguth, A., Winguth, C., 2013. Precession-driven monsoon variability at the Permian-Triassic boundary- implications for anoxia and the mass extinction. Glob. Planet.

Chang. 105, 160–170. https://doi.org/10.1016/j.gloplacha.2012.06.006.
Xie, S., Pancost, R.D., Yin, H., Wang, H., Evershed, R.P., 2005. Two episodes of microbial change coupled with Permo/Triassic faunal mass extinction. Nature 434, 494–497. https://doi.org/10.1038/nature03396.
Xie, S., Pancost, R.D., Huang, J., Wignall, P.B., Yu, J., Tang, X., Chen, L., Huang, X., Lai, X., 2007. Changes in the global carbon cycle occurred as two episodes during the Permian-Triassic crisis. Geology 35, 1083–1086. https://doi.org/10.1130/g24224a.1.
Xu, L., Lin, Y., Shen, W., Qi, L., Xie, L., Ouyang, Z., 2007. Platinum-group elements of the Meishan Permian-Triassic boundary section: evidence for flood basaltic volcanism. Chem. Geol. 246, 55–64. https://doi.org/10.1016/j.chemgeo.2007.08.013.
Yin, H., Zhang, K., Tong, J., Yang, Z., Wu, S., 2001. The global stratotype section and point (GSSP) of the Permian-Triassic boundary. Episodes 24, 102–114. http://www.stratigraphy.org/bak/Induan.pdf.
Yochelson, E.L., 1968. Biostratigraphy of the Phosphoria, Park City, and Shedhorn Formation. Geol. Surv. Prof.Paper 313-D, 571–660.
Zachos, J.C., Röhl, U., Schellenberg, S.A., Sluijs, A., Hodell, D.A., Kelly, D.C., Thomas, E., Nicolo, M., Raffi, I., Lourens, L.J., McCarren, H., Kroon, D., 2005. Rapid acidification of the ocean during the Paleocene-Eocene thermal Maximum. Science 308, 1611–1615. https://doi.org/10.1126/science.1109004.
Zhang, G., Zhang, X., Hu, D., Li, D., Algeo, T.J., Farquhar, J., Henderson, C.M., Qin, L., Shen, M., Shen, D., Schoepfer, S.D., Chen, K., Shen, Y., 2017. Redox chemistry changes in the Panthalassic Ocean linked to the end-Permian mass extinction and delayed early Triassic biotic recovery. Proc. Natl. Acad. Sci. U. S. A. 114, 1806–1810. https://doi.org/10.1073/pnas.1610931114.